The Meteoritical Society

Meteoritics & Planetary Science 61, Nr 3, 522–547 (2026)
doi: 10.1111/maps.70110

Al-Khadhaf: The first camera-observed (H5–6) meteorite fall from Oman

Anna ZAPPATINI[1]*, Edwin GNOS[2], Beda A. HOFMANN[1,3], Urs EGGENBERGER[1], Pascal M. KRUTTASCH[1], Frank GFELLER[1], Mohammad TAUSEEF[4], Ingo LEYA[4], Hadrien A. R. DEVILLEPOIX[5,6], Eleanor K. SANSOM[6], Martin CUPÁK[5], Sophie E. DEAM[5], Thomas W. C. STEVENSON[5], Peter JENNISKENS[7,8], Sebastian LINDEMANN[9], Beat BOOZ[10], Muati. S. AL-MUATI[11], Abdulmunaim A. AL-ZAKWANI[11], and Hussain A. AL-GHAFRI[11]

[1]Institute of Geological Sciences, University of Bern, Bern, Switzerland
[2]Muséum d'histoire Naturelle, Genève, Switzerland
[3]Naturhistorisches Museum Bern, Bern, Switzerland
[4]Physics Institute, Space Science and Planetology, University of Bern, Bern, Switzerland
[5]Space Science and Technology Centre, Curtin University, Perth, Western Australia, Australia
[6]International Centre for Radio Astronomy Research, Curtin University, Perth, Western Australia, Australia
[7]SETI Institute, Mountain View, California, USA
[8]NASA Ames Research Center, Moffett Field, California, USA
[9]Physics Institute, University of Freiburg, Freiburg, Germany
[10]Fachgruppe Meteorastronomie (FMA), Frick, Switzerland
[11]Ministry of Heritage and Tourism, Muscat, Sultanate of Oman

***Correspondence**
Anna Zappatini, Institute of Geological Sciences, University of Bern, Baltzerstrasse 1+3, CH-3012, Bern, Switzerland.
Email: anna.zappatini@unibe.ch

(Received 01 September 2025; revision accepted 02 February 2026)

Abstract–A fireball camera system installed in 2022 by the Oman Meteorite Monitoring Project (OMMP) as part of the Global Fireball Observatory (GFO) recorded a 3.2 s fireball on March 8, 2022 at 8:15 p.m. UTC. A meteoroid of 4 ± 2 kg entered the atmosphere at 14.0 km/s. Its trajectory, with a slope of 68.4°, started at 67.6 km and ended at 30.2 km where the meteoroid traveled at 7.36 km/s. Approximately 50 g survived atmospheric entry. On February 7, 2023, two meteorites of 13.85 g and 8.21 g were recovered at the predicted site. Gamma spectrometry confirmed their young terrestrial age via short-lived cosmogenic radionuclides ^{54}Mn and ^{22}Na. Al-Khadhaf is thus the first camera-observed meteorite fall from Oman. Petrography and mineral composition classify it as an ordinary H5–6 S2 W1 chondrite. Its pre-impact orbit ($a = 1.72$ AU, $e = 0.45$, $i = 4.36°$) is consistent with asteroid-belt delivery, with both inner-belt and Koronis-family sources remaining plausible. The cosmic ray exposure age of 8.57 ± 1.2 Ma coincides with an exposure-age peak observed among H chondrites. Al-Khadhaf adds to the record of camera-observed falls, linking meteorite compositions to their solar system context via orbit calculations.

INTRODUCTION

Earth is constantly impacted by material from space. When a large enough mass encounters Earth's atmosphere, its rapid deceleration and ablation cause the emission of light, a phenomenon called a meteor or "shooting star." Large meteors known as fireballs occasionally produce meteorites that can be found on the ground. Camera systems dedicated to observing fireballs allow for the targeted search of meteorites that were freshly delivered to Earth. Such fireball observation systems also provide insight into the frequency of meteors and enable the calculation of delivery orbits of meteoroids. They thus help to establish links between meteorite compositions and an orbit around the Sun (Jenniskens, 2014). In recent years, the number of camera-observed meteorites has steadily increased due to widespread development of fireball observation systems (e.g., Bland, 2004; Boaca et al., 2022; Borovička, Spurný, Shrbený, Štork, et al., 2022; Ceplecha et al., 1987; Colas et al., 2020; Gardiol et al., 2020; Gritsevich et al., 2014; Halliday et al., 1978, 1996; Howie, Paxman, Bland, Towner, Cupak, et al., 2017; Kokhirova et al., 2015; Li et al., 2024; Oberst et al., 1998; Spurný et al., 2006; Trigo-Rodríguez et al., 2006; Vida et al., 2021; Weryk et al., 2008; Wetherill & ReVelle, 1981; Wiśniewski et al., 2017). Currently, there exist >75 camera-observed falls with a modeled orbit (see Hlobik and Tóth (2024) and Jenniskens and Devillepoix (2025) for reviews).

When considering both the human- and camera-observed falls recovered to date, the statistics are skewed toward recovering mainly the large events and masses compared to the assumed/modeled impact frequencies (Bland et al., 1996; Shober et al., 2025). Large fireballs are more widely noticed, and the related meteorites are more easily found. To recover small meteorites, the search conditions are improved by, for example, flat, uniform terrain devoid of dark terrestrial rocks, clear weather, and lack of vegetation. Large stretches of the desert areas on the Arabian Peninsula meet those criteria. More than 20 years of meteorite searching in Oman (Hofmann and Gnos, 2024) have shown that the desert of the interior of Oman provides surfaces to retrieve even small meteorites and thus is a suitable location for the installation of a fireball observation system.

In 2022, four fireball camera systems were deployed in Oman as part of the Global Fireball Observatory (GFO) (Devillepoix et al., 2020), creating the Oman Meteorite Monitoring Project (OMMP). In 2024, two additional cameras were installed, expanding the system to six cameras. The camera locations are shown in Figure 1. The network of OMMP covers a surface of approximately 210,000 km^2.

Here, we report the first recovered (paired) meteorites from a fireball recorded by two cameras of the OMMP network. The meteorites were found on February 7, 2023, about 1 year after the fall, and show slight weathering. We present gamma-ray cosmogenic nuclide data that indicate these meteorites fell at around the time of the observed fireball. We describe their composition and texture, examine the meteoroid's history before entering the atmosphere using noble gas and ^{14}C isotopic data, and discuss its possible source region in the asteroid belt.

METHODS

The GFO Fireball Camera System

The Desert Fireball Network (DFN) of Curtin University, Australia developed and provided the camera systems (Bland, 2004; Bland et al., 2012; Howie, Paxman, Bland, Towner, Cupak, et al., 2017; Howie, Paxman, Bland, Towner, Sansom, & Devillepoix, 2017; Sansom et al., 2020; Towner et al., 2020). The DFNEXT camera system is designed for desert climates, using low-power electronics and heat-resistant components to ensure reliable operation in the hot conditions of Australia and Oman. The construction relies mainly on off-the-shelf parts, facilitating maintenance and repair. Each camera system contains a Nikon D810 DSLR, equipped with a Samyang 8 mm f/3.5 UMC Fish-eye CS II lens, which takes 27 s long-exposure images from sunset to sunrise. A LC-Tec X-FOS liquid crystal shutter splits fireball streaks into short and long segments of 0.1 s each using a de Bruijn sequence for exact timing. The camera is controlled by an embedded PC and microcontroller. GPS provides location data, and a mobile router with SIM connects it to the network. Images are stored on the PC SSD and archived daily to HDDs. During daytime processing, the on-site PC identifies potential fireball events. Bright or fast-moving streaks are flagged and sent to a central server in Australia. There, events are corroborated across multiple observatories, and false positives such as satellites, aircraft, or stray lights are removed. Positive detections trigger retrieval of fireball and calibration images, which are uploaded to the network's detection server. In parallel to photographic capturing of images, a video camera enclosed in the system supports detection of fragmentations and daytime fireballs. Detailed descriptions of the system are provided by Howie, Paxman, Bland, Towner, Cupak, et al. (2017) and Devillepoix et al. (2020).

Astrometric Calibration and Trajectory Calculations

The coordinates of the fireball shutter segments are manually picked with a custom software tool. Meteoroid positions are calibrated using the starfield in each image by comparing visible stars to a catalog (Sansom et al., 2020). The trajectory is then calibrated with these (star) pixels in combination with the camera calibration data and each observatory's altitude and coordinates. Trajectory and dark flight calculations are performed independently by different collaborators primarily to increase confidence in the predicted fall area during the meteorite search. Using two independent approaches ensures that potential systematic biases in one method would not compromise the recovery effort. Coauthor

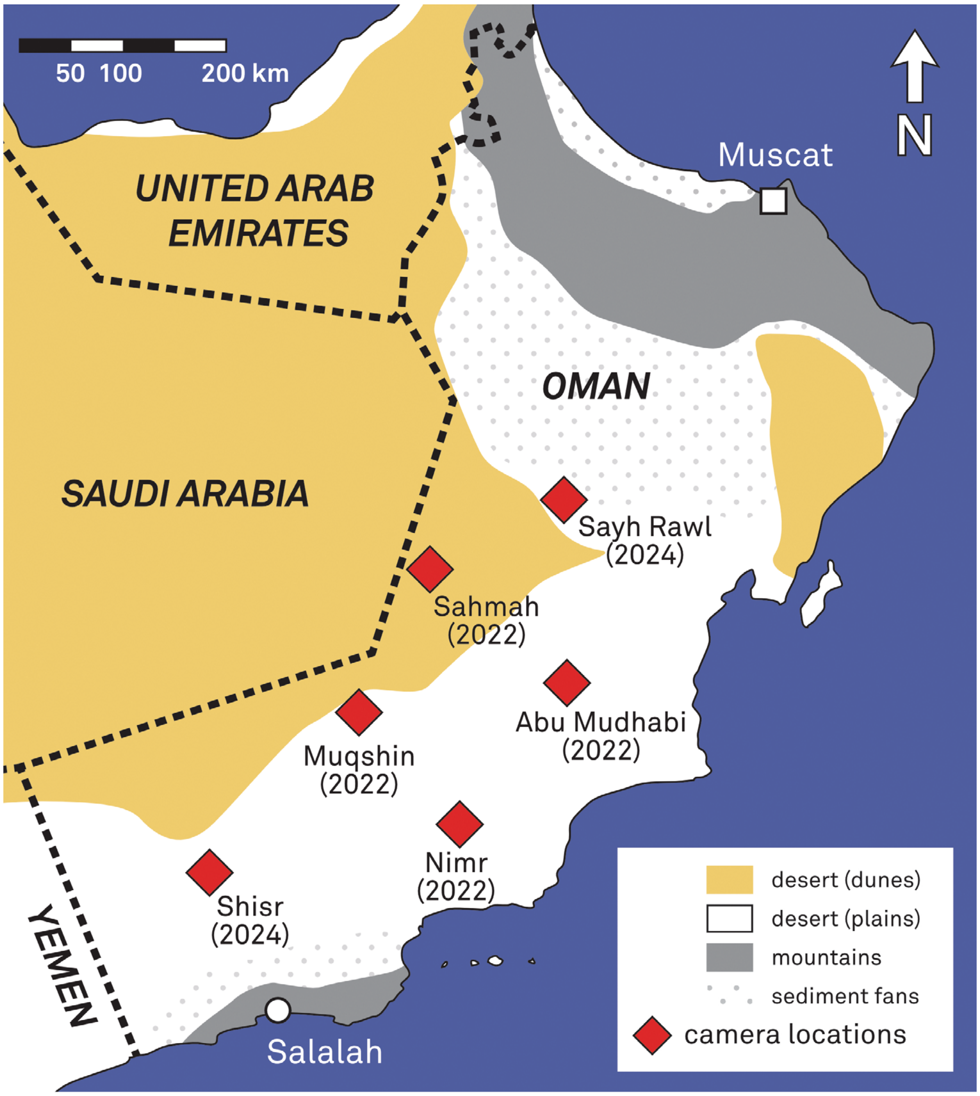

FIGURE 1. Camera locations of the OMMP as of 2025. The year in which each camera was installed is given in brackets. (Color figure can be viewed at wileyonlinelibrary.com)

Beat Booz calculates a mean trajectory from the track point coordinates using Ceplecha (1987) and performs ablation calculations using the single-mass model of Turchak and Gritsevich (2014). The DFN team performs preliminary triangulation of the observable fireball trajectory with a straight-line least-squares method (Borovička, 1990) refined with a Kalman filter and smoother to determine meteoroid position, mass, and velocity along the path (Sansom et al., 2015). The Kalman filter solution provides the meteoroid velocity as a continuous function of time and altitude along the observed trajectory. These velocity data, together with the atmospheric density profile, were used to compute the dynamic (ram) pressure $p = \rho v^2$ along the trajectory. For consistency with recent treatments, the Spreiter number was implicitly assumed to be unity (Dowling & Bradley, 2023). Whether a meteorite survived is assessed using the α–β criterion using the dimensionless ballistic (α) and mass loss (β) parameters (Gritsevich, 2009; Lyytinen & Gritsevich, 2016). The bulk ablation coefficient σ_b (in kg/MJ) was determined based on the definition in Gritsevich (2008):

$$\sigma_b = \frac{2\beta}{(1-\mu)V_e^2} \tag{1}$$

where μ corresponds to the dimensionless rotational shape factor and V_e is the entry velocity of the meteoroid in km/s. The meteoroid's pre-atmospheric orbit is calculated from the trajectory using the integration method described in Jansen-Sturgeon et al. (2019).

Photometry and Light Curve

Photometry is not routinely performed by the GFO. Here, aperture photometry is performed on each shutter break by measuring the sum pixel intensity in the green channel after local background subtraction. The result is normalized to the effective exposure time for each break and corrected to take atmospheric extinction into account following Vida et al. (2021). In the same manner, aperture photometry is performed on the high-SNR stars present in the calibration image. The intensities are normalized to the stars' effective exposure, corrected for atmospheric extinction, and combined with the star catalog V-band magnitude values; this gives us the zero-point of the system. The zero point is applied to derive apparent out-of-atmosphere magnitudes. After the triangulation step, once the observation range is known, the apparent magnitudes are converted to absolute magnitudes (normalized to 100 km distance).

The signal of the flux relative to the noise, the uncertainty in the zero point magnitude calibration, and distance uncertainty are accounted for when determining the uncertainty in absolute magnitude. Photometric mass is calculated by integrating under the light curve following Equation (2):

$$m = \int \frac{2}{\tau(v)v^2} I(t)dt \tag{2}$$

where τ is the luminous efficiency and v is the velocity (m/s) (Ceplecha et al., 1998). $I(t)$ is the total luminosity ($10^{-7}W$), which can be calculated from the absolute magnitude in the visible wavelength range M_V (here we used the green channel of the CCD) with the conversion between total luminosity I and magnitude-based luminosity I_V assuming an ablation temperature of 4000K (Equation 3).

$$I_V = 10^{-0.4M_V} \tag{3}$$

$$I/I_V = 1.95 \times 10^{10}$$

As in Borovička, Spurný, and Shrbený (2022), we use the velocity dependent luminous efficiency equation from ReVelle and Ceplecha (2001) using the parameters derived for type I meteors (ordinary chondrite material) (Equation 4).

$$\ln(\tau) = 0.465 - 10.307\ln(v) + 9.781(\ln v)^2 - 3.0414(\ln v)^3 + 0.3213(\ln v)^4 \tag{4}$$

for $v < 25.372$ km/s, where τ is the luminous efficiency in percent and v is the velocity in km/s. Knowing the luminous efficiency can vary between fireballs (see Drolshagen et al. (2021) and references within), we let $\tau(v)$ vary by a factor of 2 from that of Equation (4), to give an uncertainty of the photometric mass.

Dark Flight Modeling

The position, velocity, and mass of the meteoroid at the end of the luminous trajectory are used as initial conditions for modeling the subsequent dark flight phase, during which atmospheric winds exert a dominant control on the flight path. Because only two locations in Oman (Salalah and Muscat) provide routine atmospheric soundings, time- and location-specific atmospheric conditions are reconstructed using numerical weather modeling. Atmospheric conditions are modeled numerically using the Weather Research and Forecasting (WRF) model version 4.4 with dynamic solver ARW (Advanced Research WRF) (Skamarock et al., 2019) using global snapshots available at the National Centers For Environmental Prediction (NCEP/NOAA, 2000) as forcing data. Three simulations start at different times before the meteorite fall (on March 8, 2022 at 6:00 a.m., 12:00 p.m., and 6:00 p.m.) and compute wind speed, direction, pressure, temperature, and relative humidity up to 30 km. The model employs four nested domains with horizontal grid sizes of 27, 9, 3, and 1 km, respectively, an outer domain size of 72×72 grid cells, ($\sim$1944 $\times$ 1944 km^2), and 34 vertical levels. Planetary boundary layer physics are treated using the YSU scheme and bl_pbl_physics = 1 for all domain levels.

Dark flight trajectories are explored by the DFN team using a constrained Monte Carlo approach (Towner et al., 2022). First, astrometric uncertainties are sampled by calculating 120 trajectory solutions in which the measured astrometry is varied within its uncertainties, yielding an uncertainty ellipse at the terminal point of the luminous trajectory with standard deviations of approximately 300 m (east–west) and 80 m (north–south). These variations provide the positional uncertainty input to the dark flight modeling. To assess the sensitivity of the predicted fall area to physical assumptions, a series of dark flight simulations are performed by varying meteoroid mass, shape, and rotation state, and by comparing different drag formulations. The influence of atmospheric uncertainty is assessed by comparing fall lines obtained using the three independent WRF wind simulations. The combined results are then used to manually define operational 1σ and 2σ search regions to guide the recovery campaign. Differences between wind models lead to lateral shifts of up to ∼150 m for hypothetical ~10 g fragments, which is small compared to the overall extent of the predicted strewn field. Co-author Beat Booz calculates two dark flight variants to guide the meteorite search: one using drag coefficients from Carter et al. (2011) with variations in mass, shape, and rotation, and another using Ceplecha (1987) with unconstrained mass to predict a single impact point.

Systematic Searching of Meteorites

Seven people systematically search the area surrounding the calculated fall locations on foot, walking parallel at a distance of 10 m from each other. One person navigates along predefined GPS tracks, and flags mark the walked track approximately every 100 m; flags are collected on the return passage.

Meteorite Analysis

Magnetic susceptibility is measured with an SM30 magnetic susceptibility meter (ZH Instruments, Brno, Czech Republic). The instrument determines the apparent mass-specific susceptibility by comparing the frequency shift obtained in contact with the sample to a blank measurement in air. Values are reported as the decimal logarithm of mass-specific susceptibility, log(χ) in 10^{-9} m^3/kg, following the convention of Gattacceca et al. (2004). The correction for sample volume was applied according to the same procedure. For meteorite 23_0010, three measurements were taken, and 23_0011 was measured four times.

The 3-D shape and volume of the meteorites are determined by X-ray tomography using a SkyScan 1273 micro-CT instrument at the Institute of Geological Sciences of the University of Bern, operated at 130 keV and 115 μA. A Cu filter (2 mm) is inserted between the source and the sample to reduce beam hardening. Alignment and flat field corrections are applied before acquisition. Raw attenuation images are obtained by rotating the object over 360° with a step-size of 0.25°. Raw images are made by averaging 10 successive acquisitions, each of them using an exposure time of 1040 ms. The total scan duration is approximately 6 h. Reconstruction of 1564 slice images is performed using the program NRecon version 1.7.5.1. Corrections for misalignment, ring artifacts, and beam hardening are applied. The final voxel size on the reconstructed image is 20 μm, allowing the interpretation of any feature larger than ~100 μm. Further image analysis is performed using the Dragonfly software, Version 2021.1 for Windows (Comet Technologies Canada Inc). The bulk volume and surface area of each specimen were computed from the segmented 3-D reconstructions in Dragonfly. The voxel size of 20 μm ensures a geometric precision better than ~1% for samples of this size. Considering segmentation and thresholding uncertainties, the overall uncertainty of the derived surfaces and volumes is estimated to be within 3–5%. Bulk densities and porosities were then calculated from the measured masses and CT-derived volumes.

Radioisotopes were measured nondestructively using gamma-spectrometry at the low-background GeMSE (**Ge**rmanium **M**aterial and Meteorite **S**creening **E**xperiment) facility, located in the Vue-des-Alpes highway tunnel near Neuchâtel, Switzerland (Ramírez et al., 2022; Rosén et al., 2021; Sivers et al., 2016). The 270 m sedimentary rock overburden reduces the cosmogenic muon flux. GeMSE employs a coaxial p-type high-purity germanium crystal housed in an ultralow-background copper cryostat cooled with liquid nitrogen. The sample cavity is shielded from ambient radioactivity by layers of oxygen-free copper and low-activity lead and is purged using boil-off nitrogen to remove radon. Two large plastic scintillator panels monitor muons. Using the anti-coincidence technique, time intervals corresponding to muon detections are excluded from the measurement. The facility's low background enables detection of radioisotopes at levels of a few tens of μBq/kg. Data evaluation was performed by counting peak areas after subtraction of background counts. Because the spectrometer does not detect every decay due to particle interactions and geometry, detector efficiency is simulated using the Monte Carlo toolkit GEANT4 (Agostinelli et al., 2003; Allison et al., 2006, 2016), incorporating a 3-D model of the detector and of the meteorite derived from X-ray tomography (Ramírez et al., 2022), using average density and bulk composition of H chondrites (Wasson & Kallemeyn, 1988). The standard uncertainty for the calculated activities considers the propagated uncertainties of the peak area calculation, efficiency simulation, decay correction, and the error of the half-life.

Cosmogenic ^{14}C activity concentration measurements for Al-Khadhaf stone 23_0011 follow Tauseef et al. (2025). The $^{14}CO_2$ gas extraction and measurement techniques follow the standard procedure of the meteorite ^{14}C lab at the Physics Institute, University of Bern (Mészáros et al., 2018).

Noble gas measurements are performed at the Noble Gas Lab at Physics Institute, University of Bern. Two powdered samples of approximately 50 mg of Al-Khadhaf (stone 23_0011) are measured for He, Ne, and Ar isotope intensities, from which concentrations and ratios are inferred. Details of the measurement procedure can be found, for example, in Leya et al. (2013) and Tauseef et al. (2024).

Macroscopic images are obtained with a Nikon D800E and focus stacking in Helicon Focus. Microscopy is performed with Leica MZ6 and DM4500P microscopes. Slice and thin-section images use Olympus BX51 and Keyence VHX-J20 digital microscopes.

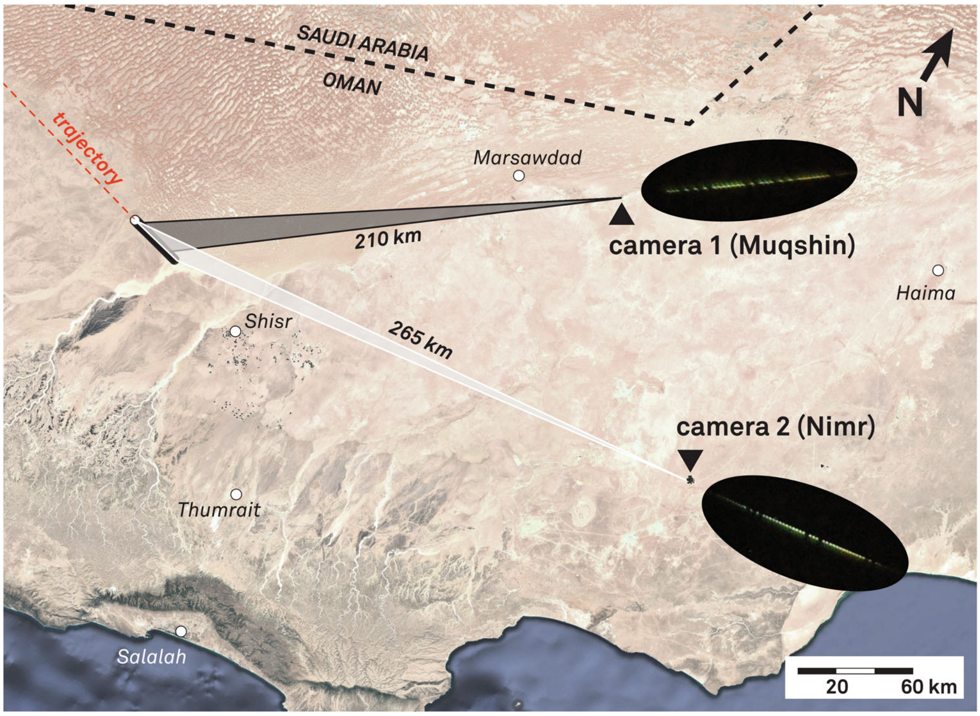

FIGURE 2. Satellite image showing the location of the two observation cameras (triangles) and the fireball trajectory. Magnified and cropped all-sky camera images of the fireball event are shown as insets. The fireball images are of the same pixel scale. Dashes encoded in the trajectories arise from the liquid crystal shutter and provide both absolute and relative timing along the trajectory. Satellite imagery: Landsat/Copernicus (2024). (Color figure can be viewed at wileyonlinelibrary.com)

TABLE 1. Trajectory parameters of the observed fireball.

Trajectory parameters	DFN beginning	DFN end	Booz beginning	Booz end
Time	20:14:54.750	20:14:57.950	20:14:54.750	20:14:57.950
Latitude (WGS84; °N)	18.50619	18.41877	18.50627	18.41883
Longitude (WGS84; °E)	53.28121	53.38346	53.27983	53.38389
Altitude (km)	67.591	30.245	67.625	30.238
Velocity (km/s)	14.00	7.36	13.95	7.77
Angle from local horizontal (°)	69.5	68.4	68.5	68.4
Calculated mass (kg)	4 ± 2[a]	0.05 ± 0.01[b]	1.04	0.035 ± 0.015
Ballistic coefficient α[b]	23.63		25.76	
Mass loss parameter β[b]	1.36		1.265	
Ablation coefficient σ (kg/MJ)[c]	0.0055		n.d.	

Abbreviation: n.d. = not determined.
[a]Calculated from the light curve.
[b]Calculated from the dynamic α, β fit (Gritsevich, 2009; Sansom, Gritsevich, et al., 2019).
[c]Determined following methods of Ceplecha (1975).

Backscatter (BSE) and secondary electron (SE) images of polished thin sections are acquired with a ZEISS EVO 50 SEM at the Institute of Geological Sciences of the University of Bern. Semiquantitative elemental analyses are performed by EDX (20 kV, 950 pA, 9–10 mm working distance) using EDAX TEAM with ZAF correction for atomic number (Z), absorption (A), and fluorescence excitation (F) effects.

Wavelength-dispersive electron microprobe (EPMA) measurements are performed using a JEOL JXA 8200 at the Institute of Geological Sciences of the University of Bern. Counting times are 10 s on background, 20 s on peak, using 15 kV acceleration voltage and 20 nA beam current. Dwell time is 90 ms. Standards include albite (Na), forsterite (Mg), anorthite (Al, Ca), orthoclase (Si, K), rutile (Ti), spinel

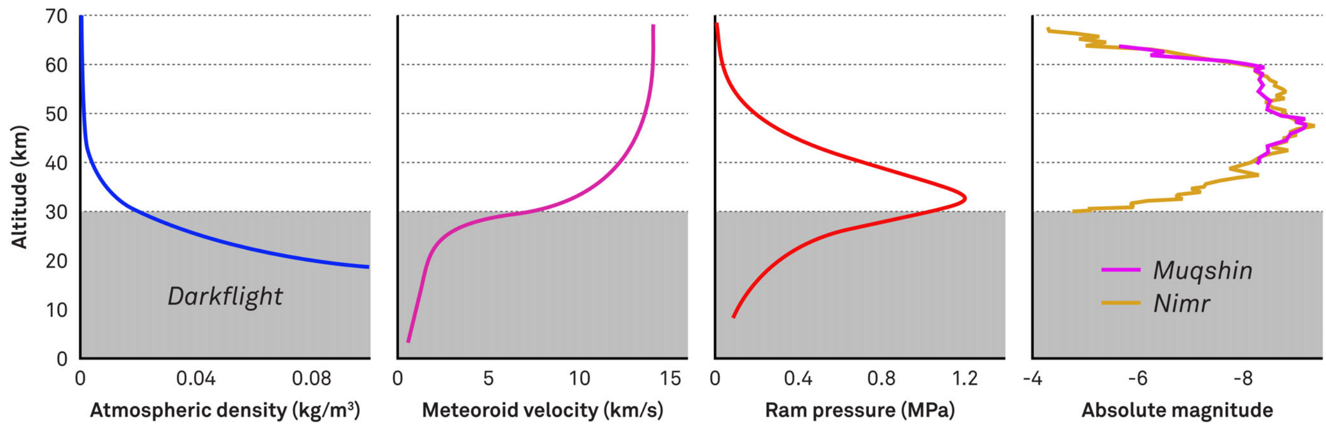

FIGURE 3. Overview of the fireball's atmospheric passage, showing atmospheric density, meteoroid velocity, dynamic (ram) pressure, and light curve as a function of altitude above ground level (DFN calculations). (Color figure can be viewed at wileyonlinelibrary.com)

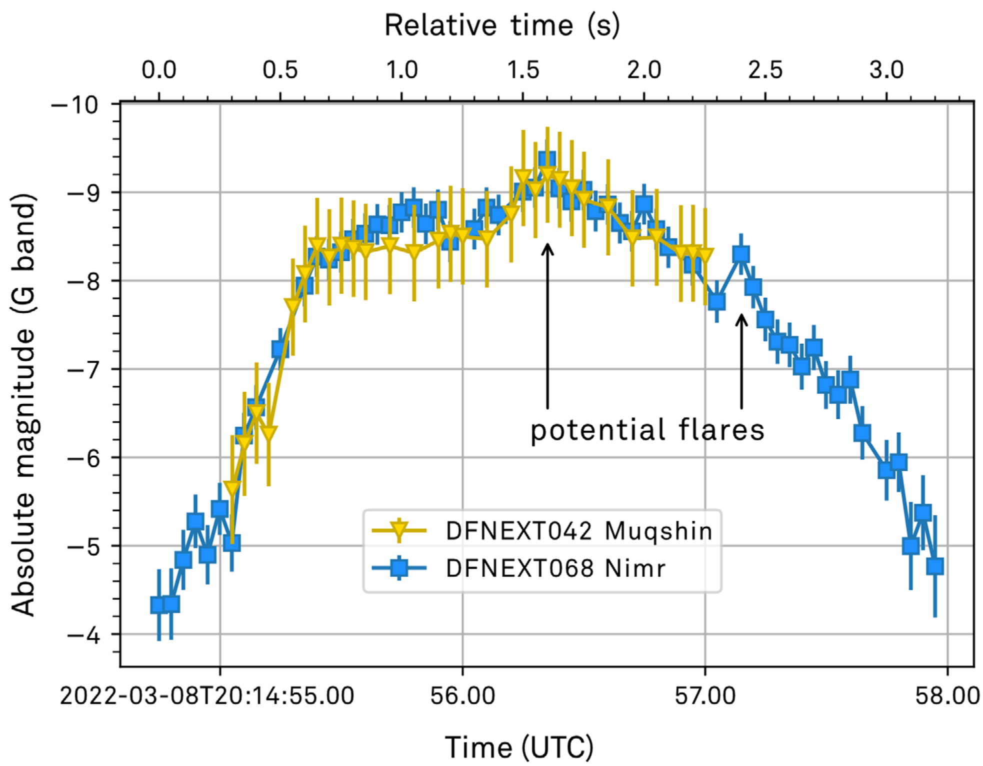

FIGURE 4. Light curve of the fireball with potential flares (luminosity surges) marked with arrows. The flares could indicate fragmentation of the meteoroid during atmospheric entry. (Color figure can be viewed at wileyonlinelibrary.com)

(Cr), pyrolusite (Mn), magnetite (Fe), and native nickel (Ni).

RESULTS

Meteoroid Trajectory and Orbit

Two of the then four fireball cameras in Oman (Muqshin and Nimr) observed a fireball on March 8, 2022 8:14:55 p.m. UTC from distances of 210 and 265 km, respectively. The geometry of the fireball relative to the cameras is shown in Figure 2, along with the corresponding fireball photos. In total, the cameras recorded 32 intervals of the de Bruijn encoded shutter sequence, corresponding to an observable duration of 3.2 s. Normally, part of the fireball would have been lost during the 3 s break between long-exposure images that is required for saving the data. However, one camera

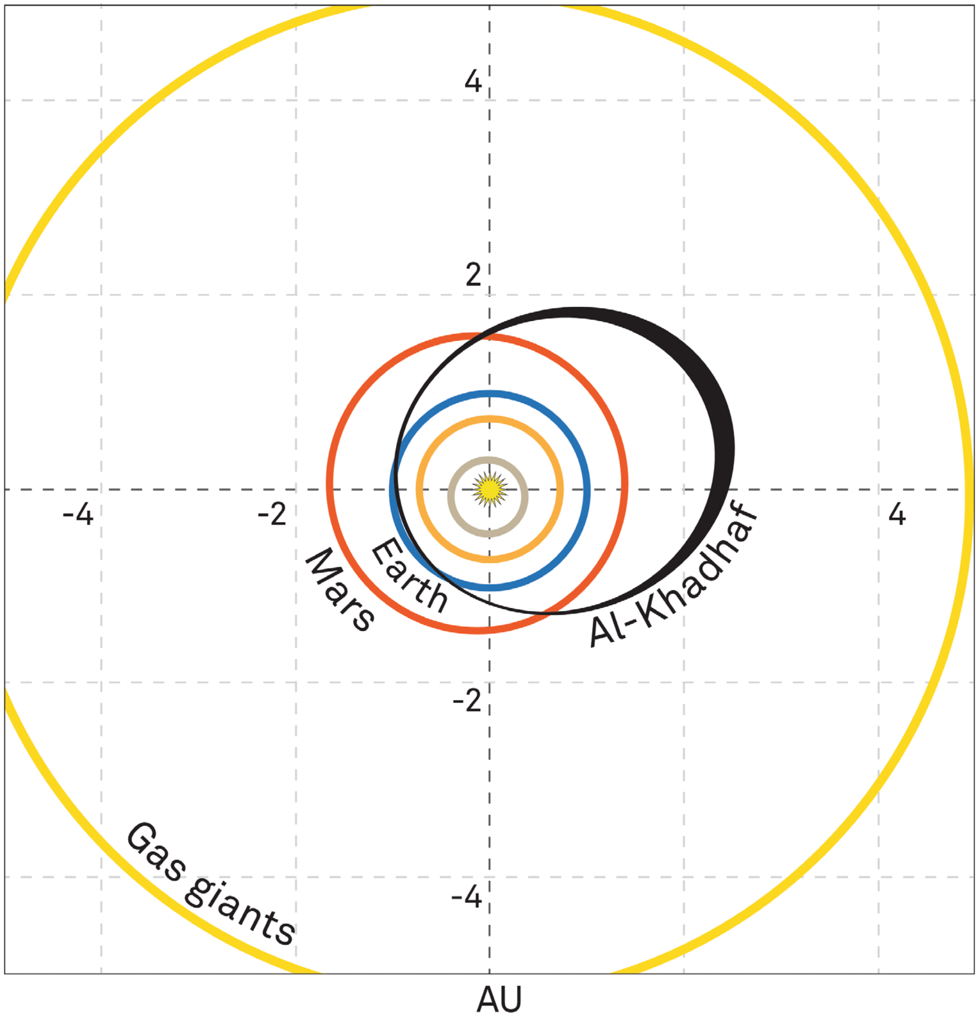

FIGURE 5. Delivery orbit of Al-Khadhaf (DFN calculations). The orbit of Al-Khadhaf is consistent with delivery from the asteroid belt. (Color figure can be viewed at wileyonlinelibrary.com)

(Nimr) was operating on incorrect GPS time information, which caused its recording to be shifted relative to Muqshin. This timing offset meant that the two cameras captured complementary parts of the fireball, together covering the full event. The fireball parameters are summarized in Table 1. The ballistic (α) and mass loss (β) parameters calculated for this fireball indicate that the event likely produced a meteorite (Gritsevich et al., 2012; Sansom, Jansen-Sturgeon, et al., 2019).

The evolution of the meteoroid's physical parameters along the trajectory is shown in Figure 3. The meteoroid decelerated progressively from an initial velocity of 14.0 km/s to 7.36 km/s at the last observed point. Combined with the atmospheric density profile, this yields a maximum dynamic pressure of 1.17 MPa, reached shortly before the end of the luminous trajectory.

The light curve of the fireball, shown in Figure 4, did not saturate the sensors—a rare case for a meteorite-dropping event. This provided an unusually high-quality record of the fireball's brightness, from which we estimate a photometric mass of around 4 ± 2 kg. Given the light curve's quality, the main source of uncertainty lies in the luminous efficiency and the assumptions therein (e.g., Subasinghe et al. (2017) and Drolshagen et al. (2021)). Using the average density of the finally found meteorites (3.35 g/cm^3), the photometric mass of 4 ± 2 kg corresponds to a sphere with a diameter of ~10–15 cm. We also used the mass estimation method of Johnston and Stern (2024), which links the ablation of an intact meteoroid directly to its diameter, disregarding other meteoroid properties. Al-Khadhaf's initial size was at the low end of the given range to use this method (diameter $>$ 10 cm) and gave a much larger estimated diameter of 25 cm.

Monte Carlo orbit regression places the meteoroid in a heliocentric orbit interior to the main asteroid belt, with

TABLE 2. Orbital parameters expressed in the heliocentric ecliptic frame (J2000) and associated 1σ formal uncertainties.

Orbital parameters	DFN	Booz
Epoch (TDB)	2022-03-08	2022-03-08
Semi-major axis a (AU)	1.722 ± 0.021	1.743
Eccentricity e	0.451 ± 0.007	0.457
Inclination i (°)	4.36 ± 0.06	4.00
Argument of perihelion ω (°)	212.25 ± 0.17	211.19
Longitude of the ascending node Ω (°)	347.974 ± 0.002	347.936
Perihelion distance q (AU)	0.945 ± 0.001	0.948
Aphelion distance Q (AU)	2.499 ± 0.043	2.539
Corrected radiant (RA) α (°)	138.79 ± 0.13	136.85
Corrected radiant (Dec) δ_g (°)	34.74 ± 0.05	31.96
Geocentric speed V_g (km/s)	8.69 ± 0.14	8.61
Tisserand parameter (wrt. Jupiter)	4.05 ± 0.04	4.01

a semi-major axis of 1.72 AU. The pre-atmospheric orbit is shown in Figure 5, with orbital parameters listed in Table 2. Two independent trajectory and orbit solutions are reported in Tables 1 and 2, derived separately by the DFN team and by B. Booz using slightly different assumptions regarding timing, reference frames, and initial velocity. These solutions are not intended to represent competing final results, but rather to document the independent analyses that were carried out during the meteorite recovery effort. Both solutions were based on the same astrometric observations and produced consistent dark flight predictions, which increased confidence in the predicted fall area.

Dark Flight and Wind Modeling

The final observed point of the trajectory is at 18.418766° N, 53.383456° E, at an altitude of 30.245 km (above the WGS84 ellipsoid). At this stage, the meteoroid traveled at 7.36 km/s with a slope of 68.44° relative to the local horizontal. These values were used to initialize the dark flight calculations. All three atmospheric weather models produced broadly similar results, except for fragments below 10 g, where differences in the predicted locations of ~150 m can be observed. Figure 6 shows a 1D vertical section of one of the weather models, defined by the location of the calculated end point of the bright flight. The data tables of all the models are available as supplementary material. The WRF models indicate mild easterly winds at high altitudes (<15 m/s at 20–30 km) and stronger northerly winds at lower altitudes (~30 m/s at 5–20 km) (Figure 6). At high levels, winds oppose the fall direction and shorten the target area. Closer to the ground, northerly winds bend the fall lines southward, most notably for low masses (Figure 7).

End-mass modeling suggested that a small meteorite survived atmospheric entry. The alpha–beta dynamical fit (Sansom, Gritsevich, et al., 2019) was consistent with a 50–250 g meteorite surviving at the last observed point (assuming 3.5 g/cm^3 density, allowing for shapes ranging from sphere to brick). The Kalman filter (Sansom et al., 2015) gave a consistent estimate of ~50 g (assuming 3.5 g/cm^3 density and spherical shape). The cameras were not close enough and sensitive enough to observe the end of the bright flight. Hence, the dark flight code modeled the mass lost due to the unobserved ablation, taking the final estimate at the start of true dark flight to ~30–200 g, assuming no further fragmentation had happened.

Dark flight modeling by the DFN team assuming a spherical meteorite shape places the 50 g mass at 18.369082° N, 53.435664° E. A parallel calculation using the WRF weather model (Booz) predicted a landing point ~100 m away, at 18.370078° N, 53.435321° E. The close match between these independent calculations is shown in Figure 7. When instead using balloon data from Salalah, the 50 g mass was projected to fall ~700 m further west. The modeled fall area lies northwest of Shisr, at the border of the Rub' Al Khali dunes. It is a gravel plain with patches of sand, scattered small dunes, and sparse vegetation.

Meteorite Recovery

The 2σ target area for the meteorite search shown in Figure 7 corresponds to 0.6 km^2. In 2 days, about 1.3 km^2 were thoroughly searched systematically by seven people. On February 7, 2023, two meteorites were recovered 395 m apart, one close to the calculated fall line and the other about 390 m away, near the edge of the modeled strewn field (Figure 7). The larger piece (field number 23_0010) was found on a sandy flat with few visual distractions (Figure 8). The second (field number 23_0011) was recovered on sand between small dunes with scattered *Calotropis procera*, *Citrullus colocynthis*, and *Calligonum* shrubs. Coordinates for both specimens are listed in Table 3. The find location lies 12.2 km southwest of a small desert camp named Al-Khadhaf. Al-Khadhaf is Arabic for "camels starting to accelerate and run when reaching an open flat area after passing mountains or dunes."

Physical Properties, Petrography, and Mineralogy

The two specimens weigh 13.851 g and 8.214 g, respectively, resulting in a total mass of 22.065 g. Magnetic susceptibilities, as well as volumes, surface

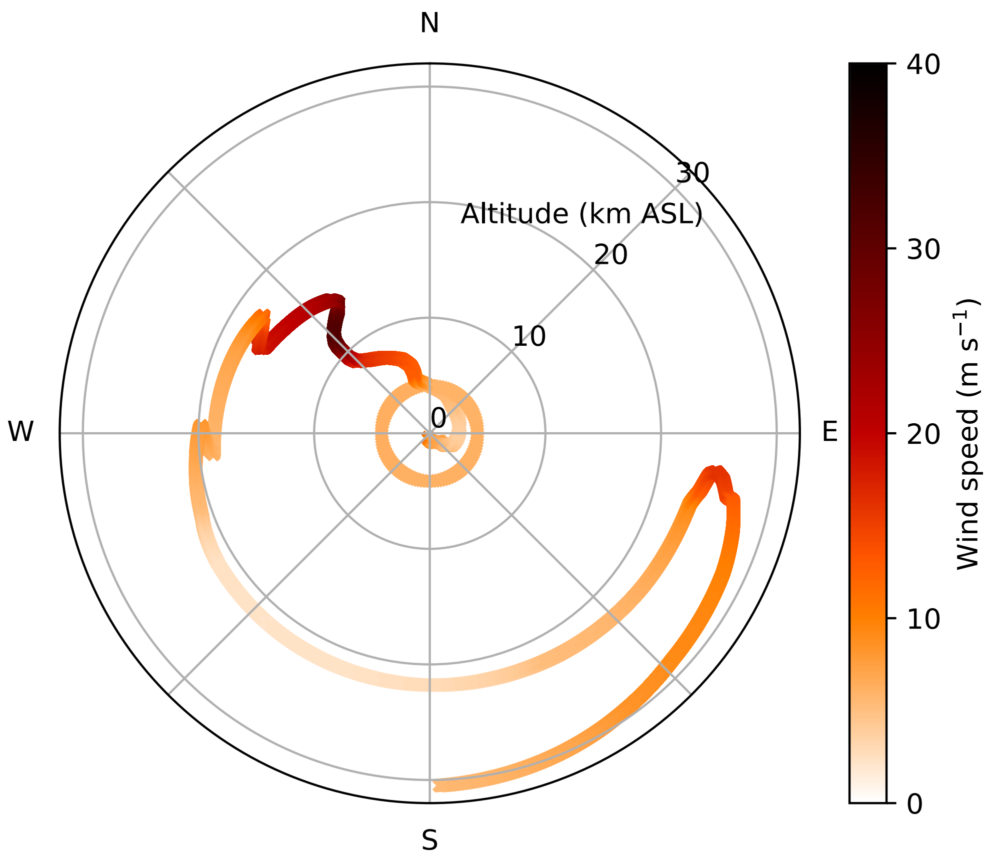

FIGURE 6. Wind profiles showing wind direction and wind speed at the time of the meteor, as modeled by WRF. Prevailing easterly winds at high altitudes and northerly winds at lower altitudes affected the flight of the meteorites. (Color figure can be viewed at wileyonlinelibrary.com)

areas, and bulk densities inferred from X-ray tomography, are listed in Table 3.

The larger fragment (23_0010) is pyramid-shaped, while the smaller (23_0011) has an elongated, slightly curved form (Figure 8). The fusion crust is dark gray-black, crosscut by fine cracks, and partially covers broken surfaces where chondrules and unaltered silicates are visible. Rust occurs around metal and sulfide grains on these surfaces. Cut sections reveal a brecciated texture containing both mineral and rock fragments (Figure 9).

Both samples are crosscut by shock veins composed mainly of opaque phases and fine-grained clasts. Metal and sulfides are partly altered to iron (hydr)oxides, especially along cracks that follow the veins. Chondrules and fragments are sparse but reach 0.2–0.5 mm in size. Chondrule types include barred olivine, radial pyroxene, and porphyritic pyroxene and olivine. The mineralogy is dominated by olivine, pyroxene, plagioclase, and abundant metal and sulfide. Chromite, merrillite, and ilmenite occur in trace amounts. The recrystallized matrix contains mineral clasts of variable grain size. Feldspar ranges from 5 to 50 μm in diameter, and a large clast (3 × 5 mm) in the bigger sample contains coarse plagioclase (>50 μm) (Figure 10). The fusion crust shows vesicles and a mesh of fine sulfide veins. Undulose extinction as a shock indicator is widespread, but no planar fractures were observed.

Average mineral compositions of both specimens and the coarse clast, determined by EPMA, are given in Table 4. Detailed analyses are available as supplementary material. The compositions are homogeneous with small standard deviations, whether the meteorites are considered individually or as a combined data set.

Gamma Spectrometry

The short-lived cosmogenic radionuclides ^{54}Mn ($t_{1/2} = 0.86$ a) and ^{22}Na ($t_{1/2} = 2.60$ a), expected in meteorites that fell within the past year, were detected in both samples (Figure 11). The activity of the long-lived cosmogenic nuclide ^{26}Al constrains the pre-atmospheric diameter of the meteoroid to <8 cm using the modeled production rates of Leya et al. (2021). ^{40}K was also analyzed to complement the compositional data. Activities of all relevant radionuclides are summarized in

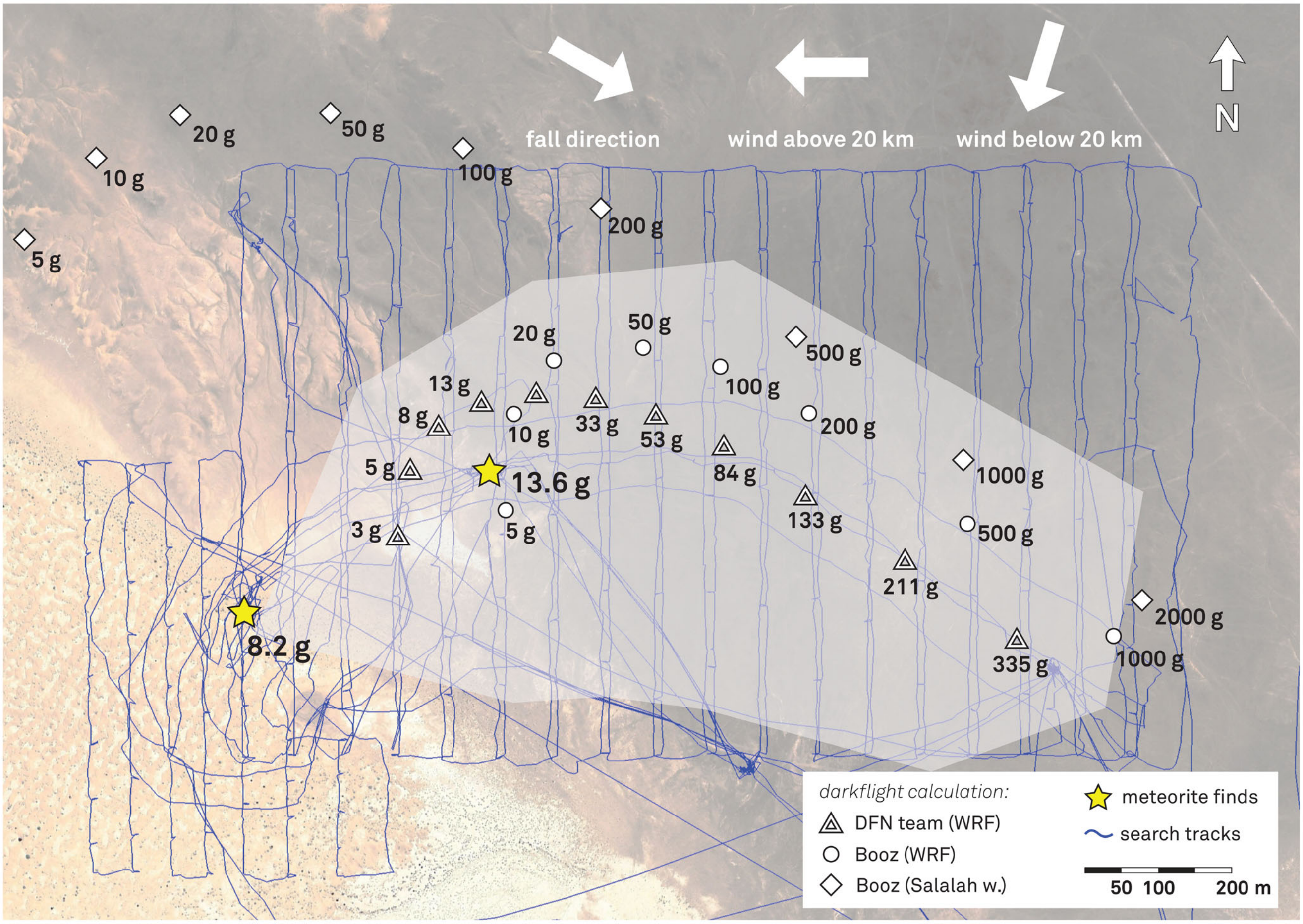

FIGURE 7. Satellite image of the target area showing the modeled fall lines and strewn field derived by the DFN and by Booz, together with the search tracks (thin blue lines) and the find locations of the two meteorites. The shaded area corresponds to the operational 2σ search region defined by the DFN team. Satellite imagery: Landsat/Copernicus (2024). (Color figure can be viewed at wileyonlinelibrary.com)

Table 5. To allow comparability between the two samples despite not measuring them simultaneously, activities are reported for the time of the fall.

Calculating terrestrial ages from short-lived radionuclides is difficult because their initial activities are hard to constrain. Besides depending on the pre-atmospheric size of the meteoroid and the shielding depth of the sample, production rates also vary with the solar cycle. During phases of high solar activity, the solar wind reduces the flux of galactic cosmic rays, which suppresses the production of nuclides formed mainly by high-energy galactic particles. This leads to an anticorrelation between sunspots and production rates (Evans et al., 1982). This effect is often corrected for by normalizing the short-lived radionuclides to ^{26}Al. In Al-Khadhaf, however, ^{26}Al activity is particularly low, resulting in high ^{22}Na /^{26}Al and ^{54}Mn/^{26}Al ratios compared to other meteorite falls from similar phases of the 11-year solar cycle (Figure 12).

Carbon-14 and Terrestrial Age

The ^{14}C production rate of Al-Khadhaf reported by Tauseef et al. (2024) is 23.2 ± 0.4 dpm/kg. Figure 13 plots the expected ^{14}C production rates against the shielding depth indicator $(^{22}Ne/^{21}Ne)_{cos}$ for 11 H chondrite falls including Al-Khadhaf. Al-Khadhaf falls close to the best-fit line. These observations point to a terrestrial age of $<$300 years and are consistent with a recent fall.

Noble Gases and Cosmic Ray Exposure Age

The measured noble gas isotopic concentrations and ratios are shown in Tables 6 and 7. Data from the aliquot Al-Khadhaf–1 as reported by Tauseef et al. (2025) is also included for completeness. The Ne isotopic ratios (^{20}Ne/^{22}Ne = 0.844, 0.829, 0.910 and ^{21}Ne/^{22}Ne = 0.801, 0.812, 0.798) indicate cosmogenic Ne with no or only minor trapped contributions. In a ^{20}Ne/^{22}Ne versus

FIGURE 8. Images at the top and bottom show the landscapes of the two find locations of 23_0010 (top) and 23_0011 (bottom) and field and studio photos of the two recovered meteorites (Studio photos by Thomas Schüpbach). Note that the larger stone is an oriented meteorite. (Color figure can be viewed at wileyonlinelibrary.com)

$^{21}Ne/^{22}Ne$ plot (Figure 14), all aliquots plot in the field of cosmogenic gases. Also shown is data for ordinary chondrites from Mahajan (2022) and Tauseef et al. (2024, 2025). Cosmogenic Ne determined by two-component deconvolution using air ($^{20}Ne/^{22}Ne = 9.8$, $^{21}Ne/^{22}Ne = 0.02878$) and cosmogenic gases ($^{20}Ne/^{22}Ne = 0.81$) as endmembers yields $(^{22}Ne/^{21}Ne)_{cos}$ of 1.244, 1.230, and 1.243, indicating a likely pre-atmospheric size of <10 cm in diameter, as inferred following Leya and Masarik (2009) and Tauseef et al. (2024).

TABLE 3. Summarized properties of the two recovered meteorite samples.

	23_0010	23_0011
Find Latitude (WGS84; °N)	18.36857	18.36682
Find Longitude (WGS84; °E)	53.43335	53.43015
Mass (g)	13.851	8.214
Volume (cm^3)	4.17 ± 0.21	2.44 ± 0.12
Bulk density (g/cm^3)	3.32 ± 0.16	3.37 ± 0.17
Surface area (cm^2)	19.0 ± 1.0	15.3 ± 0.8
Magnetic susceptibility log χ ($10^{-9}\ m^3/kg$)	5.24 ± 0.01	5.21 ± 0.03

Measured Ar isotopic ratios are also consistent across aliquots. The measurement of the aliquot Al-Khadhaf–1 was not successful and thus only data for Al-Khadhaf–2 and 3 are reported. These two aliquots yield $^{38}Ar/^{36}Ar$ ratios of 1.10 and 1.13, and $^{40}Ar/^{36}Ar$ ratios of 7459 and 8862. Deconvolution of cosmogenic and trapped contributions following Wieler (2002) yields $^{38}Ar_{cos}$ concentrations of 3.7×10^{-9} and $4.5 \times 10^{-9}\ cm^3$ STP/g, respectively.

The so-called "Bern plot", which displays the $(^{3}He/^{21}Ne)_{cos}$ against the $(^{22}Ne/^{21}Ne)_{cos}$ (Figure 15) can be used as an indicator of thermal ^{3}He loss (Eberhardt et al., 1966; Nishiizumi et al., 1980). The $(^{3}He/^{21}Ne)_{cos}$ (8.13, 7.67, and 6.57) and $(^{22}Ne/^{21}Ne)_{cos}$ (1.244, 1.230, and 1.243) place all three aliquots of Al-Khadhaf within the 15% variation envelope of the empirical correlation.

Based on the cosmogenic components, individual CRE ages were determined for all aliquots (Table 7). The $^{3}He_{cos}$ ages (T_3) are 7.35 ± 0.8, 6.23 ± 1.0, and 6.69 ± 0.9 Ma for Al-Khadhaf–1, 2, and 3, respectively. Corresponding $^{21}Ne_{cos}$ ages (T_{21}) are 8.53 ± 0.9, 7.50 ± 0.8, and 9.62 ± 1.7 Ma. For $^{38}Ar_{cos}$, ages could be calculated for Al-Khadhaf–2 and 3 only, yielding 8.95 ± 2.1 and 10.9 ± 2.1 Ma. The average ages calculated over all measured nuclides for the three aliquots (T_{avg}) are 7.89 ± 0.6, 7.28 ± 0.6, and 8.17 ± 0.7 Ma for Al-Khadhaf–1, 2, and 3, respectively. Based on the ^{21}Ne ages, which are generally regarded as the most reliable, the average CRE age of Al-Khadhaf is 8.57 ± 1.2 Ma.

DISCUSSION

Mineral compositions, textures, and magnetic properties are consistent with an equilibrated, brecciated H-group ordinary chondrite. The comparatively low fayalite (Fa) and ferrosilite (Fs) contents (Table 4) are

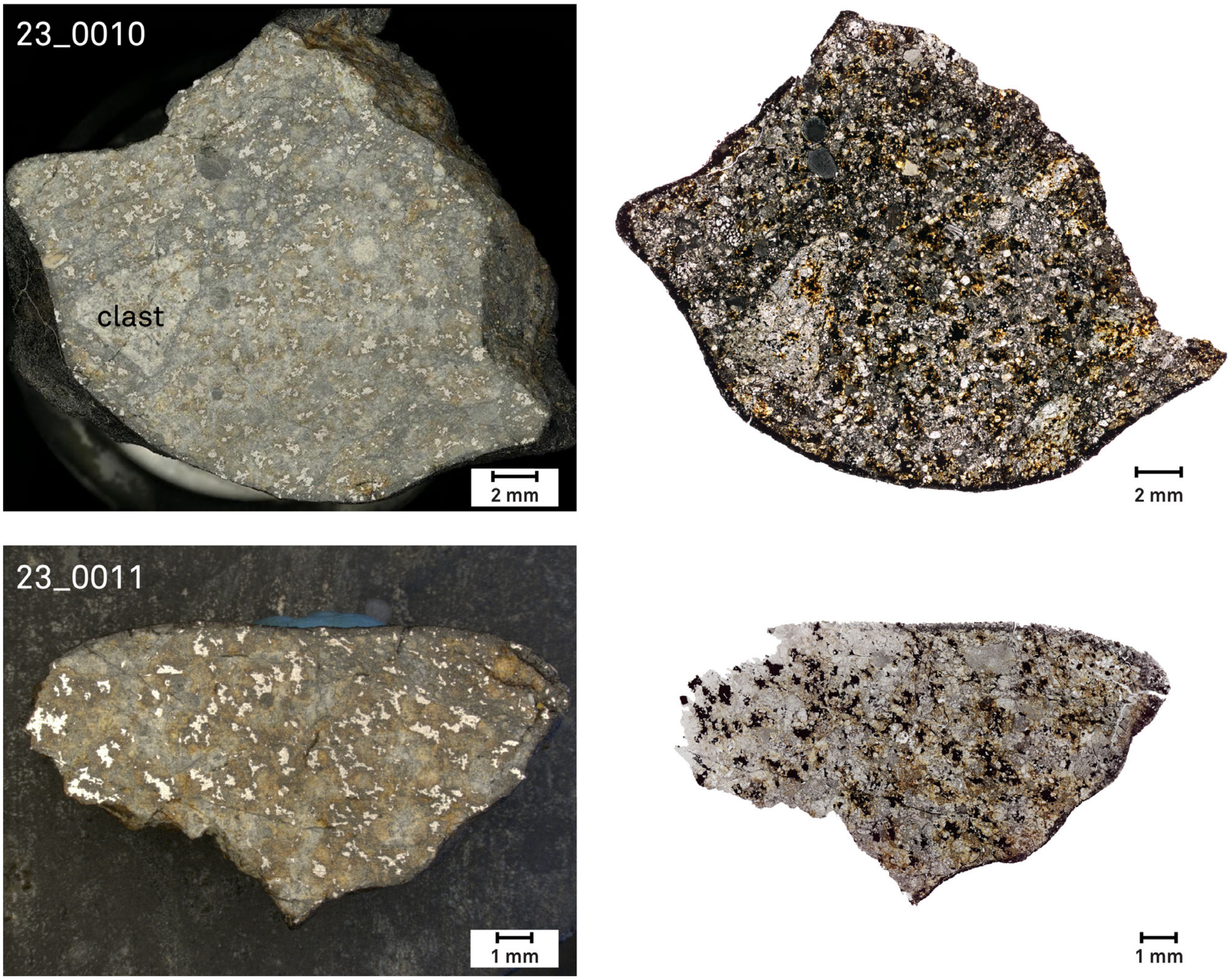

FIGURE 9. Images of cut slabs (left) and thin sections (right, plane-polarized light) of both pieces of Al-Khadhaf. The sawn surface shows bright metal/sulfide grains, chondrules, angular clasts, and darker silicate matrix. Incipient rust appears as reddish hues around the metal/sulfide grains. (Color figure can be viewed at wileyonlinelibrary.com)

characteristic of H chondrites. The crystalline matrix, visible chondrule delineation, and matrix plagioclase grain sizes of 2–50 μm indicate a dominant petrologic type 5, whereas a clast containing coarser plagioclase (>50 μm) but identical mineral chemistry corresponds to type 6 material (Figure 10). Undulose extinction of silicates without mosaicism or planar fractures indicates a moderate shock stage (S2). Slight alteration of metal and sulfide phases points to a low weathering degree (W1). As the meteorite exhibits the archetypical features of ordinary chondrites, oxygen isotope analyses were deemed unnecessary. Overall, the meteorite is classified as a brecciated H5–6 (S2, W1) ordinary chondrite.

The presence of fusion crust on broken surfaces indicates secondary fragmentation of the meteoroid late in flight. The matching appearance, texture, mineral compositions, and short-lived radionuclide activities of both recovered fragments confirm that they belong to the same fall event. The mineralogy of the clast closely matches that of the host material, implying that both parts stem from a similar parent body. The petrographic grade of 5–6 is further supported by the absence of trapped Ne, typical of higher grade ordinary chondrites that have lost such components during metamorphism (Dalcher et al., 2013; Wieler, 2002). Localized shock veins indicate one or several moderate impact events affecting the meteoroid that partially melted sulfides and produced limited grain-size reduction of adjacent silicates. Whether the clast is truly derived from the same parent body and was incorporated during the initial formation of the meteoroid or whether it is the result of a later collision between meteoroids of similar composition remains uncertain.

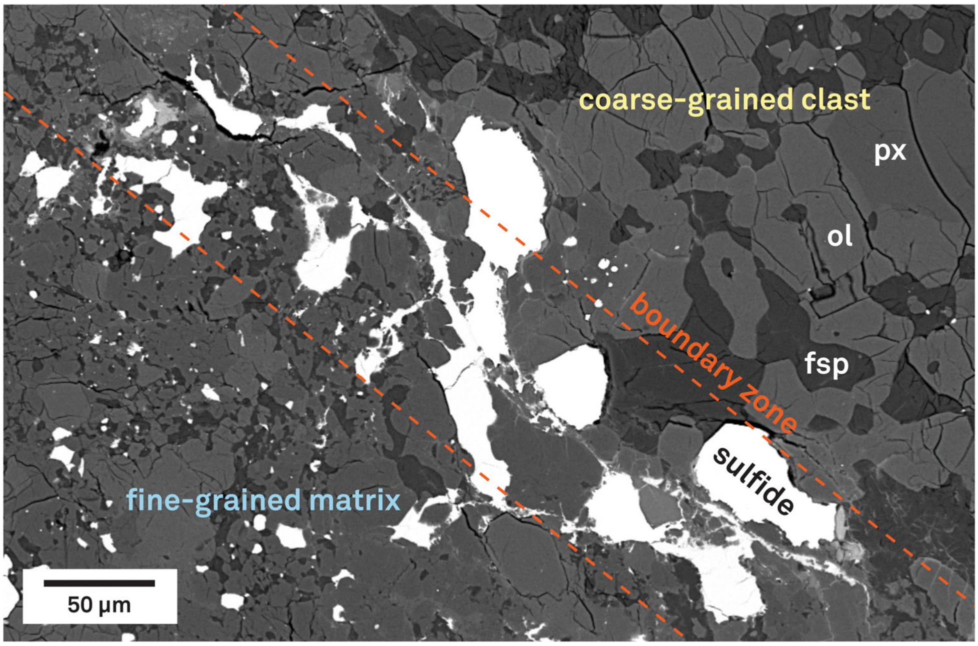

FIGURE 10. Backscatter electron image of the interface between clast and matrix in 23_0010. A sulfide vein-rich zone marks the boundary between the coarser grained clast and the finer grained matrix. px = pyroxene, ol = olivine, fsp = feldspar. (Color figure can be viewed at wileyonlinelibrary.com)

Association with Observed Fall

The presence of the short-lived cosmogenic radionuclides ^{54}Mn ($t_{½} = 0.86$ a) and ^{22}Na ($t_{½} = 2.60$ a) confirms that Al-Khadhaf is a recent fall and that both meteorites (23_0010 and 23_0011) are paired. Considering that Al-Khadhaf fell during the rising phase of solar cycle 25, the ^{26}Al-normalized activities of ^{54}Mn and ^{22}Na for Al-Khadhaf are somewhat higher than expected. This is attributed to the relatively low ^{26}Al activity in the samples which is discussed further below. The plot of ^{26}Al-normalized ^{54}Mn and ^{22}Na activities of other meteorite falls with published gamma-spectrometry data along the solar cycles (Figure 12) reveals a subtle anticorrelation with sunspot number, which is most apparent for solar cycle 24.

Although only two cameras recorded the fireball from distances of >200 km, trajectory calculations accurately predicted the main landing area. Independent calculations by the DFN team and B. Booz, based on the same astrometric data but differing slightly in trajectory geometry, initial velocities and reference systems, produced consistent dark flight predictions. The resulting differences in radiant coordinates and orbital elements therefore reflect methodological choices rather than incompatible solutions, and both were sufficient to guide a successful recovery. Both predictions based on WRF weather data placed the meteorite closest to the actual find locations, while the weather balloon-based models predicted slightly more displaced fall lines.

The two recovered masses were consistent with the lower estimate of the modeled final mass. The final fragmentation likely occurred shortly before the onset of dark flight, as indicated by the presence of thin fusion crusts on the broken surfaces. This interpretation is supported by the trajectory-derived dynamic pressure profile, which reaches a maximum of 1.17 MPa shortly before the end of the luminous flight (Figure 3).

The maximum dynamic pressure of 1.17 MPa can be compared to published measurements of the mechanical strength of ordinary chondritic material. Laboratory measurements on ordinary chondrite samples indicate quasi-static compressive strengths of tens to hundreds of MPa, with tensile strengths generally an order of magnitude lower (Kimberley & Ramesh, 2011; Pohl & Britt, 2020; Popova et al., 2011). However, atmospheric fragmentation is observed to occur at much lower dynamic pressures, typically in the range of ~0.9–5 MPa for confirmed ordinary chondrite fireballs (Borovička et al., 2020), reflecting preexisting fractures and loading conditions not captured by static tests. In this context, the dynamic pressure experienced by Al-Khadhaf before the end of the luminous flight lies within the range expected for the onset of breakup in ordinary chondritic meteoroids. A local enhancement in brightness occurs near the altitude of maximum dynamic pressure (Figs 3 and 4), suggesting a possible fragmentation event.

TABLE 4. Average mineral compositions as measured by EPMA. Number of analyzed grains in parentheses.

	SiO_2	TiO_2	Al_2O_3	FeO	MnO	MgO	CaO	Na_2O	K_2O	Cr_2O_3	NiO	Total	Endm.
Pyroxene													
23_0010 ($n = 18$)	56.3 ± 0.3	0.14 ± 0.05	0.15 ± 0.05	11.1 ± 0.3	0.52 ± 0.02	31.3 ± 0.5	0.67 ± 0.08	0.02 ± 0.01	n.d.	0.15 ± 0.09	0.01 ± 0.02	100.3	$Fs_{17}Wo_1$
23_0010 clast ($n = 5$)	56.4 ± 0.4	0.14 ± 0.06	0.16 ± 0.08	11.1 ± 0.3	0.52 ± 0.01	31.2 ± 0.5	0.70 ± 0.09	0.01 ± 0.02	n.d.	0.13 ± 0.08	0.01 ± 0.02	100.3	$Fs_{17}Wo_1$
23_0011 ($n = 43$)	56.0 ± 0.4	0.16 ± 0.05	0.17 ± 0.07	11.0 ± 0.5	0.52 ± 0.02	30.3 ± 0.4	0.72 ± 0.07	0.02 ± 0.01	n.d.	0.12 ± 0.06	0.03 ± 0.03	99.2	$Fs_{17}Wo_1$
Olivine													
23_0010 ($n = 32$)	39.2 ± 0.5	0.03 ± 0.03	0.01 ± 0.01	17.5 ± 0.5	0.49 ± 0.02	43.6 ± 0.9	0.03 ± 0.02	0.01 ± 0.01	0.01 ± 0.01	0.02 ± 0.05	0.02 ± 0.06	100.7	Fa_{18}
23_0010 clast ($n = 7$)	39.4 ± 0.3	0.03 ± 0.03	0.01 ± 0.01	17.3 ± 0.6	0.50 ± 0.02	43.9 ± 0.4	0.03 ± 0.02	0.02 ± 0.02	0.01 ± 0.01	0.04 ± 0.05	0.02 ± 0.03	101.1	Fa_{18}
23_0011 ($n = 72$)	39.0 ± 0.5	0.02 ± 0.03	0.01 ± 0.02	17.1 ± 0.5	0.48 ± 0.02	42.3 ± 0.8	0.06 ± 0.02	0.01 ± 0.01	n.d.	0.02 ± 0.02	0.02 ± 0.02	99.0	Fa_{19}
Feldspar													
23_0010 ($n = 7$)	64.6 ± 1.0	0.04 ± 0.01	21.8 ± 0.3	0.62 ± 0.20	0.02 ± 0.02	0.02 ± 0.06	2.38 ± 0.11	9.64 ± 0.28	1.06 ± 0.19	0.02 ± 0.02	0.05 ± 0.06	100.2	$An_{11}Or_6$
23_0010 clast ($n = 3$)	64.5 ± 1.4	0.03 ± 0.01	21.7 ± 0.4	0.72 ± 0.23	0.01 ± 0.02	0.10 ± 0.08	2.34 ± 0.11	9.72 ± 0.36	0.99 ± 0.06	0.02 ± 0.02	0.05 ± 0.05	100.2	$An_{11}Or_6$
23_0011 ($n = 8$)	64.6 ± 0.7	0.04 ± 0.01	21.8 ± 0.3	0.39 ± 0.42	0.01 ± 0.01	0.03 ± 0.06	2.30 ± 0.21	9.29 ± 0.41	1.05 ± 0.11	0.01 ± 0.01	0.03 ± 0.06	99.5	$An_{11}Or_6$
Chromite													
23_0010 ($n = 5$)	< 0.01	2.27 ± 0.15	7.01 ± 0.26	28.6 ± 0.3	1.14 ± 0.06	3.50 ± 0.16	0.03 ± 0.03	0.03 ± 0.03	n.d.	55.4 ± 0.3	0.04 ± 0.04	98.0	
23_0011 ($n = 6$)	< 0.01	2.22 ± 0.27	7.12 ± 0.46	28.2 ± 0.6	1.23 ± 0.06	3.41 ± 0.30	0.11 ± 0.11	0.01 ± 0.02	n.d.	55.3 ± 0.8	0.03 ± 0.03	97.7	

Abbreviation: n.d. = not determined.

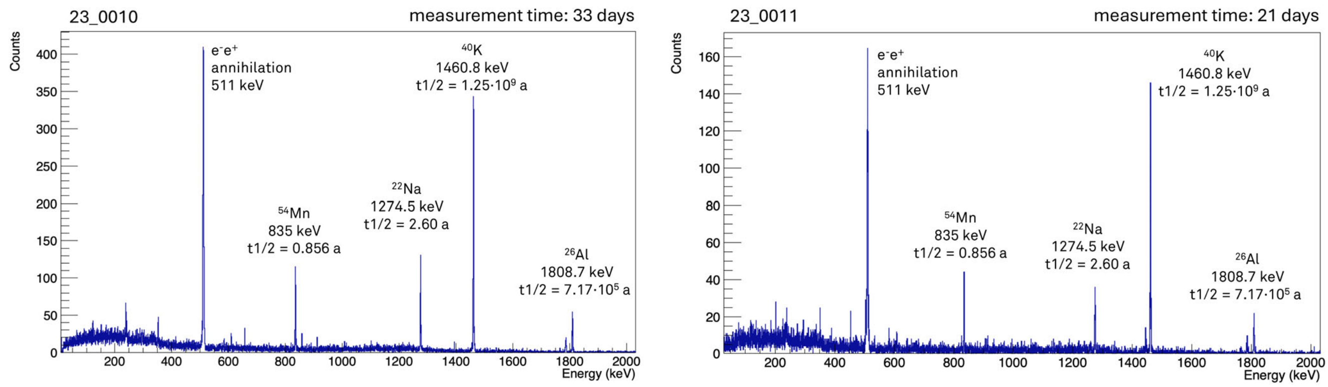

FIGURE 11. Gamma spectra of both samples. Sample 23_0010 was measured for 33 days (April 27– May 30, 2023) and 23_0011 for 21 days (April 4–27, 2023). The clear peaks of the short-lived cosmogenic radionuclides ^{54}Mn and ^{22}Na in both spectra confirm the recent fall of the meteorites. (Color figure can be viewed at wileyonlinelibrary.com)

TABLE 5. Activities of cosmogenic radionuclides and primordial ^{40}K measured by gamma spectrometry, given for the time of the fall. The given bulk K content was calculated via ^{40}K activity.

Isotope	Half-life	23_0010 (dpm/kg)	23_0011 (dpm/kg)
^{54}Mn	0.86 a	70.2 ± 1.3	70.0 ± 1.9
^{22}Na	2.60 a	83.8 ± 4.2	80.0 ± 5.3
^{26}Al	7.17×10^5 a	24.0 ± 1.8	23.8 ± 2.2
^{40}K	1.248×10^9 a	1499 ± 79	1466 ± 82
K (mg/kg)		806	777

The dynamical parameters inferred for the meteoroid's path through the atmosphere depend on the assumed atmospheric density profile along the luminous trajectory. Simplified atmospheric descriptions (e.g., exponential or standard atmospheres) can lead to noticeable differences in the ballistic coefficient α, which directly controls the altitude at which deceleration becomes apparent and thus affects dynamic mass estimates. In contrast, the mass loss parameter β is much less sensitive to the choice of atmospheric model, as it depends primarily on the initial velocity and ablation behavior (Lyytinen & Gritsevich, 2016). Using time- and location-specific atmospheric profiles derived from models such as NRLMSISE-2000/2002 (Picone et al., 2002) or WRF (Skamarock et al., 2008) can therefore refine absolute mass estimates but is not expected to significantly alter the inferred ablation efficiency or the conclusion that Al-Khadhaf was a meteorite-dropping fireball.

The smaller meteorite fragment was found 9 m outside of the 2σ target area. The reason for this is unclear. Perhaps shock–shock interactions between the fragments led to a flight vector change as described for 2008 TC_3 by Jenniskens et al. (2022) and for Winchcombe by McMullan et al. (2024). Alternatively, non-modeled subtleties in the atmospheric winds could have unexpectedly altered the flight path. The inferred survival of only a few percent of the initial mass is typical for meteorite-dropping fireballs and comparable to other small camera-observed falls such as Murrili and Arpu Kuilpu (Sansom et al., 2020; Shober et al., 2022).

Pre-atmospheric Size

The initial mass estimate of Al-Khadhaf using the method of Johnston and Stern (2024) is of much poorer quality than that obtained for the New York State fireball (McFadden et al., 2024) using the same approach: in that case, the model-derived mass agreed with the photometric one to within 23%, whereas for Al-Khadhaf, no such agreement is achieved. In contrast, the photometric initial mass of 4 ± 2 kg calculated together with the recovered total mass of 22.065 g is consistent with the ablation behavior inferred from dynamical modeling. To better constrain the pre-atmospheric size, we compare three independent approaches:

1. Light-curve integration:
   Integration of the unsaturated fireball light curve using luminous-efficiency prescriptions of Revelle and Ceplecha (2001) yields an entry mass of 4 ± 2 kg, corresponding to a diameter of about 10–15 cm.
2. Cosmogenic radionuclides (^{26}Al, ^{14}C):
   The low ^{26}Al activities (24.0 ± 1.8 and 23.8 ± 2.2 dpm/kg) imply, when compared with production rate models (Leya et al., 2021), a maximum diameter of 8 cm. This is qualitatively supported by the low ^{14}C activity concentration reported by Tauseef et al. (2025).
3. Cosmogenic noble gases $(^{22}Ne/^{21}Ne)_{cos}$:
   The shielding-sensitive $(^{22}Ne/^{21}Ne)_{cos}$ ratio is consistent with diameters >10 cm when compared with the production rates of Leya and Masarik (2009).

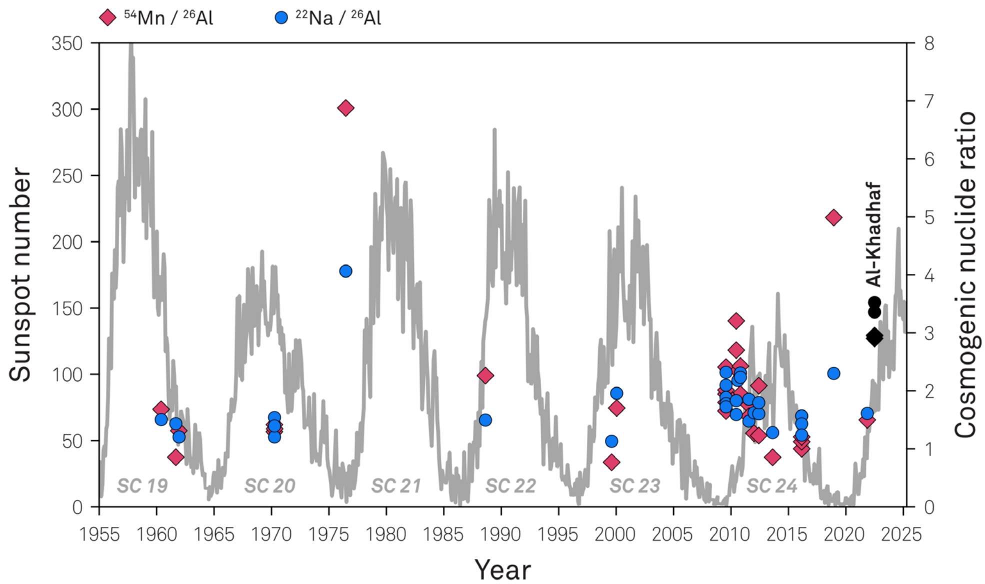

FIGURE 12. ^{54}Mn/^{22}Na and ^{22}Na /^{26}Al ratios reported for meteorite falls along the sunspot number during solar cycles 19–25 (data from the U.S. National Oceanic and Atmospheric Administration). The cosmogenic nuclide data is from Antonin, Boumdeid (Buhl et al., 2014), Braunschweig (Bartoschewitz et al., 2017), Creston (Jenniskens et al., 2019), Ehole (Honda & Arnold, 1964), Harleton (Honda & Arnold, 1964), Hammadah al Hamra 346 (Tymiński et al., 2023), Huaxi (Rosén et al., 2020), Jesenice (Bischoff et al., 2011), Kamargaon (Ray et al., 2017), Jilin (Honda et al., 1982), Kobe (Komura et al., 2002), Košice (Alexeev et al., 2015; Povinec et al., 2015), Lost City (Cressy, 1971; Wrigley, 1971), Mifflin (Kita et al., 2013), Sabrum (Ghosh et al., 2002), Søøtmany (Laubenstein et al., 2012), Torino (Bhandari et al., 1989), Ucera (Cressy, 1971), and Xining (Rosén et al., 2020). (Color figure can be viewed at wileyonlinelibrary.com)

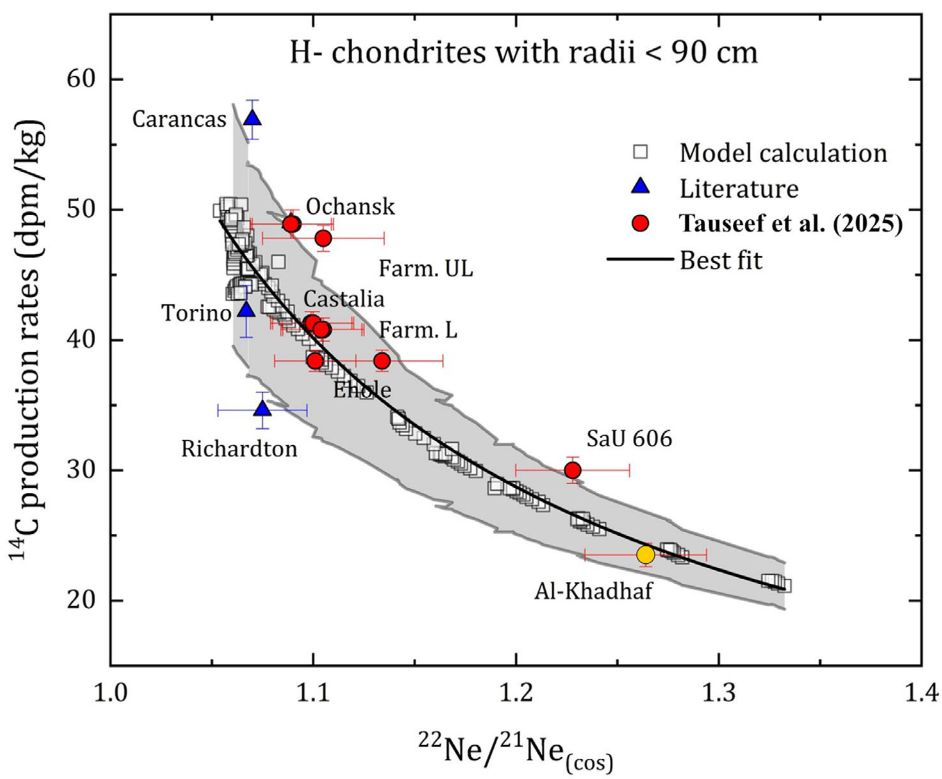

FIGURE 13. Carbon-14 production rate and cosmogenic ^{22}Ne/^{21}Ne of Al-Khadhaf compared to other H chondrites. Data from Tauseef et al. (2025). Al-Khadhaf has a low ^{14}C production rate and high (^{22}Ne/^{21}Ne)$_{cos}$, both indicators for a small pre-atmospheric radius of the meteoroid. (Color figure can be viewed at wileyonlinelibrary.com)

TABLE 6. Measured He, Ne, and Ar isotope concentrations ($\times 10^{-8}$ cm^3 STP/g) and ratios in Al-Khadhaf.

Sample ID	^{4}He	^{4}He/^{3}He	^{20}Ne	^{20}Ne/^{22}Ne	^{21}Ne/^{22}Ne	^{36}Ar	^{36}Ar/^{38}Ar	^{40}Ar/^{36}Ar
Al-Khadhaf–1[a]	1414 ± 133	127 ± 10	1.43 ± 0.08	0.844 ± 0.032	0.801 ± 0.016	n.d.	n.d.	n.d.
Al-Khadhaf–2	1514 ± 068	159 ± 18	1.68 ± 0.09	0.829 ± 0.020	0.812 ± 0.019	0.451 ± 0.108	1.10 ± 0.3	8862 ± 2230
Al-Khadhaf–3	1672 ± 076	165 ± 15	1.58 ± 0.20	0.910 ± 0.019	0.798 ± 0.020	0.568 ± 0.120	1.13 ± 0.3	7459 ± 1684

Abbreviation: n.d. = not determined.
[a]Al-Khadhaf–1 data taken from Tauseef et al. (2025). The He, Ne, and Ar isotope concentrations in Al-Khadhaf–2 and Al-Khadhaf–3 aliquots were measured in this study.

TABLE 7. Cosmogenic ^{3}He, ^{21}Ne, and ^{38}Ar concentrations ($\times 10^{-8}$ cm^3 STP/g), and CRE ages (in Ma) for Al-Khadhaf. T_{avg} are weighted averages using uncertainties as weights.

Sample ID	^{3}He$_{cos}$	^{21}Ne$_{cos}$	^{38}Ar$_{cos}$	^{3}He/^{21}Ne$_{cos}$	^{22}Ne/^{21}Ne$_{cos}$	T_3	T_{21}	T_{38}	$T_{avg.}$
Al-Khadhaf–1[a]	11.2 ± 0.9	1.36 ± 0.1	n.d.	8.13 ± 0.9	1.244 ± 0.02	7.35 ± 0.8	8.53 ± 0.9	n.d.	7.89 ± 0.6
Al-Khadhaf–2	9.5 ± 1.1	1.24 ± 0.1	0.37 ± 0.08	7.67 ± 1.1	1.230 ± 0.01	6.23 ± 1.0	7.50 ± 0.8	8.95 ± 2.1	7.28 ± 0.6
Al-Khadhaf–3	10.2 ± 1.0	1.54 ± 0.2	0.45 ± 0.09	6.57 ± 1.4	1.243 ± 0.04	6.69 ± 0.9	9.62 ± 1.7	10.9 ± 2.3	8.17 ± 0.7

Abbreviation: n.d. = not determined.
[a]Al-Khadhaf–1 data taken from Tauseef et al. (2025).

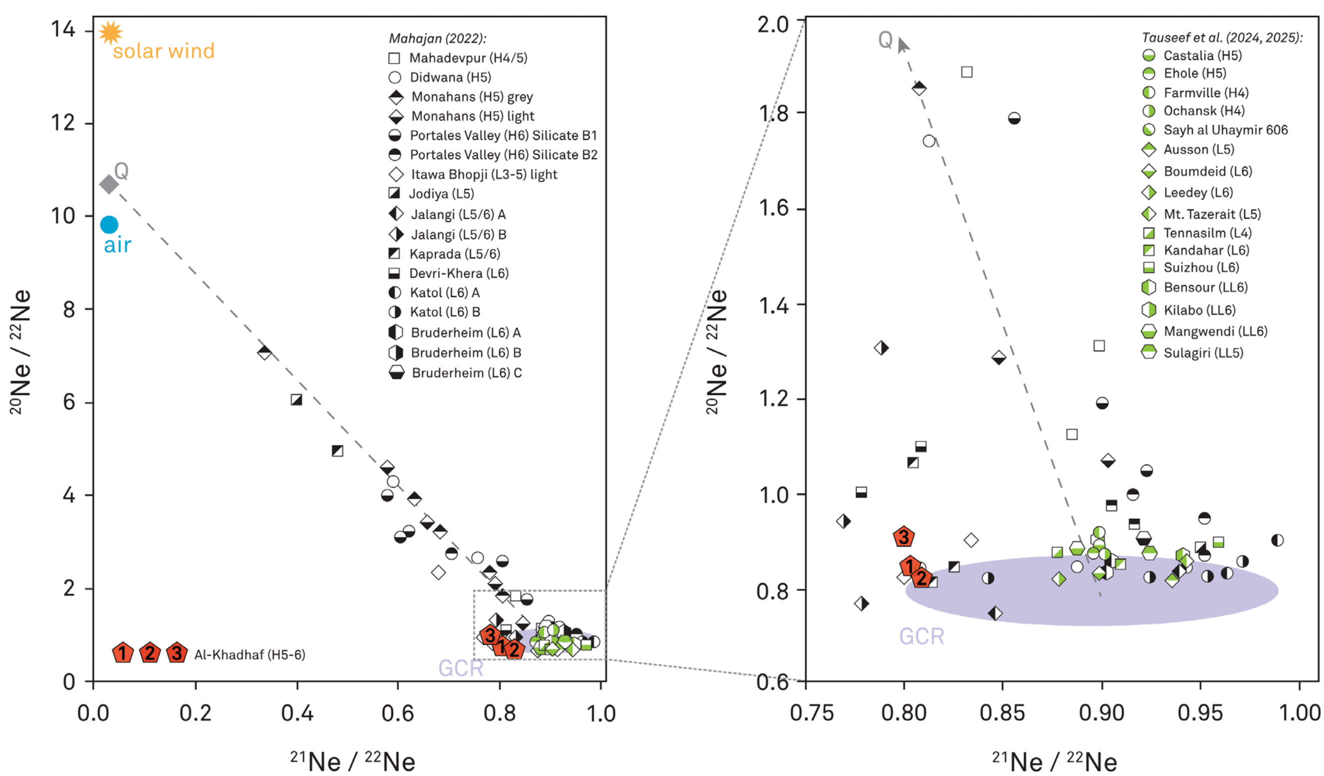

FIGURE 14. The ^{20}Ne/^{22}Ne and ^{21}Ne/^{22}Ne ratios of Al-Khadhaf (aliquots 1–3) indicate a dominant cosmogenic component. Data from Mahajan (2022) and Tauseef et al. (2024, 2025). (Color figure can be viewed at wileyonlinelibrary.com)

These methods do not converge on a single value but collectively bracket a pre-atmospheric diameter of ~5–15 cm. The spread reflects the different sensitivities and assumptions of each technique (e.g., luminous efficiency, shielding geometry and production rate, potential deviations from spherical shape). To illustrate how these independent constraints relate to one another, Figure 16 summarizes the diameter and shielding ranges inferred from the light curve, cosmogenic

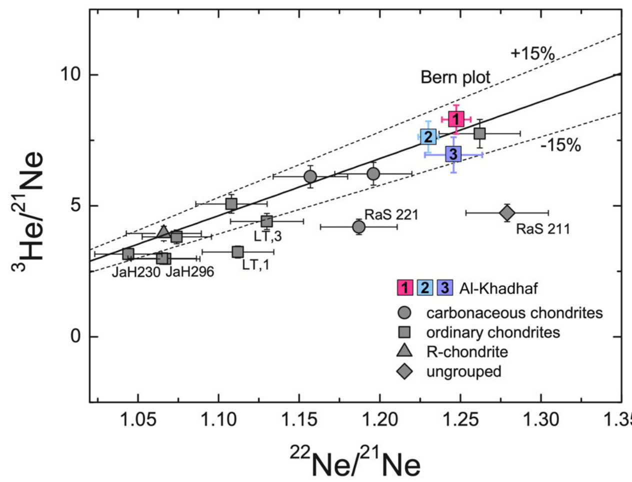

FIGURE 15. Cosmogenic $^{3}He/^{21}Ne$ plotted against cosmogenic $^{22}Ne/^{21}Ne$. The empirical correlations of Nishiizumi et al. (1980) are shown; experimental data and the original plot are from Leya et al. (2013). Al-Khadhaf aliquots 1–3 lie within the ±15% variation shown as dashed lines, indicating that ^{3}He loss due to thermal effects was minimal. (Color figure can be viewed at wileyonlinelibrary.com)

radionuclides, and cosmogenic noble gases. Because the measured cosmogenic activities fall near the lower end of available production-rate curves, a broad range of sample depths, from the surface to roughly half the diameter, remains consistent with the data. As a result, it is difficult to constrain the shielding geometry more tightly.

For context, the Cavezzo fall (Bizzarri et al., 2023; Gardiol et al., 2020) had an entry mass of 3.5 ± 0.8 kg and a pre-atmospheric diameter of ~13 cm, making it one of the smallest meteoroids recovered on the ground following instrumental observation. Al-Khadhaf's photometric entry mass of 4 ± 2 kg and pre-atmospheric diameter (10–15 cm) places it in the same size regime. Given the cosmogenic constraints that allow diameters below 8 cm, Al-Khadhaf is among the smallest camera-observed meteoroids from which meteorites have been recovered.

Source Region in the Asteroid Belt

Knowing the cosmic ray exposure (CRE) age of Al-Khadhaf is essential for understanding its space history. We derived a CRE age of 8.57 ± 1.2 Ma from the cosmogenic noble gas data. The $^{3}He_{cos}$ ages are somewhat younger than the $^{21}Ne_{cos}$ and $^{38}Ar_{cos}$ ages, which could reflect minor thermal ^{3}He loss. The alignment of Al-Khadhaf with the Bern correlation, however, indicates that any ^{3}He loss was not significant. Ages calculated from $^{38}Ar_{cos}$ are older but carry larger uncertainties. For these reasons, we consider the $^{21}Ne_{cos}$ ages the most reliable and use them to define the CRE age.

The CRE age combined with the heliocentric delivery orbit allow us to place Al-Khadhaf in context with the population of H chondrites and their possible source regions. Figure 16 shows inclination versus semi-major axis for previously observed H chondrite impact orbits, with colors indicating CRE age peaks where available. The pre-atmospheric orbit of Al-Khadhaf (star in Figure 17; orbital parameters in Table 2) has a semi-major axis of 1.72 AU and a low inclination of 4.36°, indicating that the meteoroid moved on an Earth-crossing orbit interior to the main asteroid belt. The CRE age of Al-Khadhaf lies within the main exposure age population of H chondrites (David & Leya, 2019; Graf & Marti, 1995), plotting on the outer flank of the ~7 Ma peak.

Jenniskens and Devillepoix (2025) note that this ~7 Ma peak is broader than other H-chondrite exposure-age clusters and likely represents contributions from multiple source regions. Proposed contributors include the Koronis family at low inclination beyond the 5:2 resonance and the Nele family in the central main belt. Al-Khadhaf's CRE age is higher than that typically associated with the Nele family (~6 Ma), making a Nele origin less likely. The mineral chemistry of Al-Khadhaf (Fa 17.7–19.0%, Fs 15.8–17.4%) lies near the upper end of the compositional ranges proposed for Koronis family material (Figure 18). While this places Al-Khadhaf at the margin of Koronis-like compositions (Genge, 2008; Sanchez et al., 2015), it does not exclude an origin in that family. An alternative possibility is a source in the inner main belt, such as the Massalia family. Dynamically, material released from the inner belt can be efficiently delivered to Earth via resonances such as ν6 (Nesvorný et al., 2023). However, recent spectral work by Marsset et al. (2024) suggest that the Massalia family is more closely linked to L chondrites, complicating a straightforward association with H chondrites. At the same time, reflectance spectra provide indirect constraints on mineralogy and may not uniquely map onto meteoritic compositions.

Taken together, the CRE age, orbit, and mineral chemistry of Al-Khadhaf do not uniquely identify a single source family. Both Koronis and inner-belt sources such as Massalia remain plausible contributors to the ~7 Ma H-chondrite exposure-age population. Al-Khadhaf therefore highlights the continued difficulty of linking individual meteorite falls to specific asteroid families, particularly within broad and likely multisource exposure-age clusters.

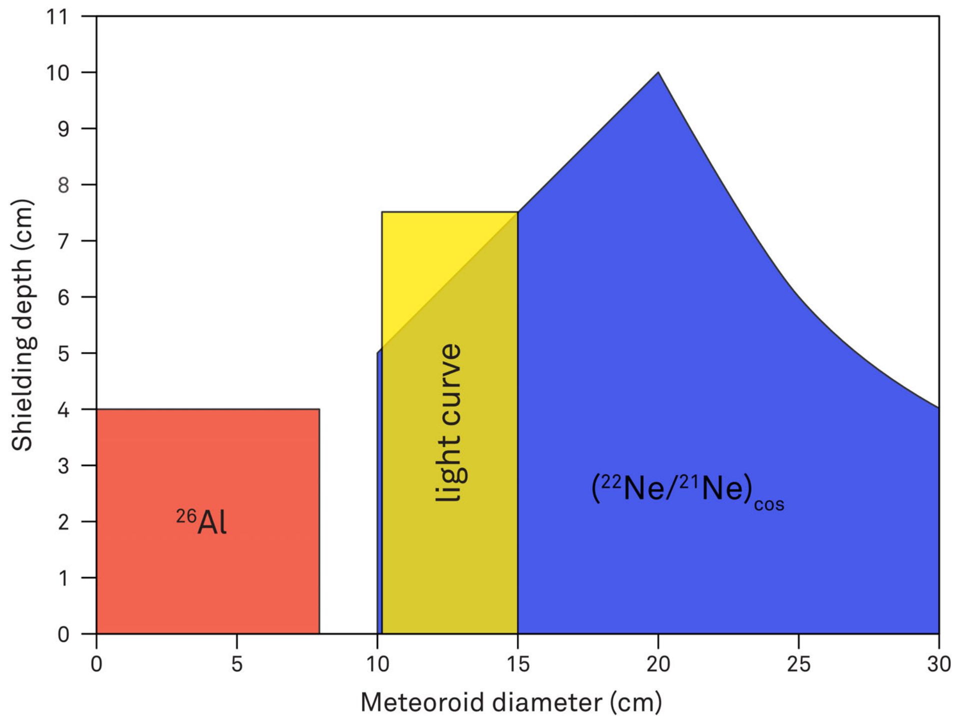

FIGURE 16. Comparison of shielding depths and pre-atmospheric diameters inferred from cosmogenic nuclides (^{26}Al, ^{22}Ne/^{21}Ne) and photometry. Although the model estimates do not overlap exactly, together they constrain the pre-atmospheric diameter of Al-Khadhaf to ~5–15 cm. (Color figure can be viewed at wileyonlinelibrary.com)

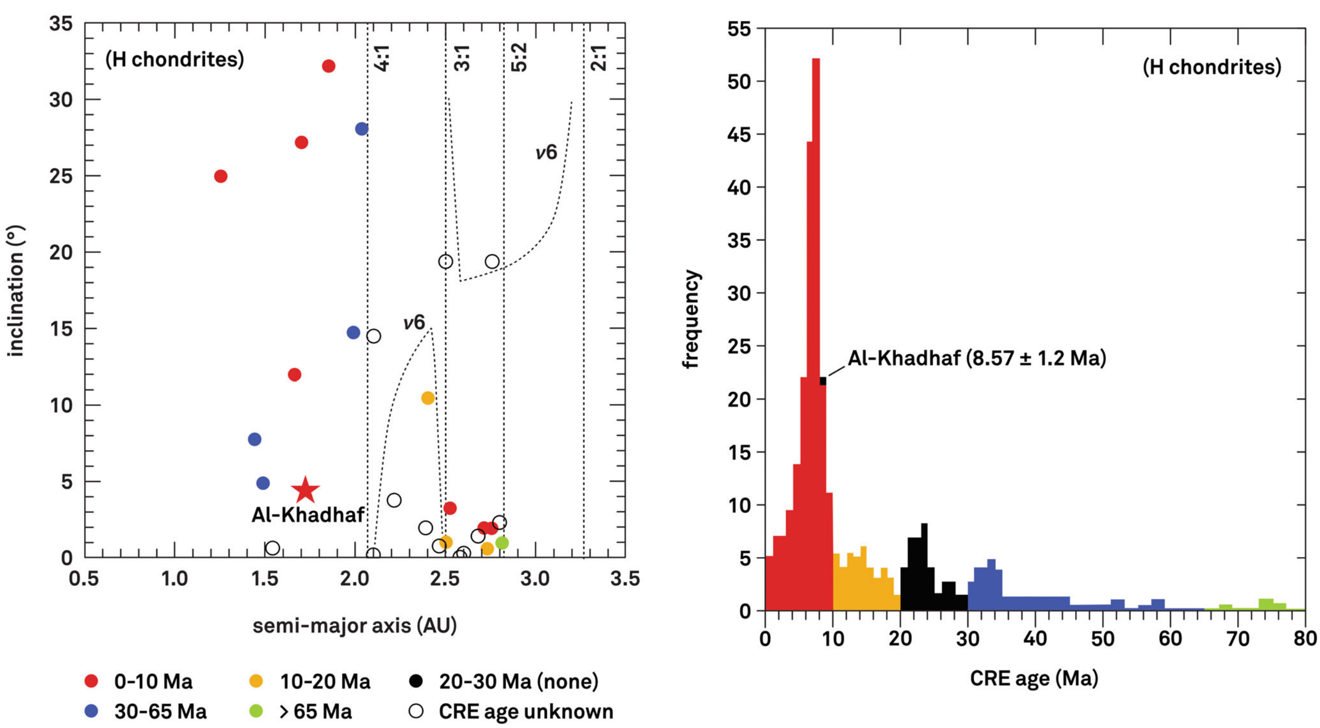

FIGURE 17. Inclination and semi-major axis of Al-Khadhaf compared to other H chondrite falls. Ratios mark orbital resonances, and color coding represents cosmic-ray exposure (CRE) ages. Al-Khadhaf's low inclination indicates an orbit only slightly tilted relative to the ecliptic, suggesting limited dynamical excitation before Earth encounter. Its CRE age lies within the main population of H-chondrite exposure ages. Modified after Jenniskens and Devillepoix (2025). (Color figure can be viewed at wileyonlinelibrary.com)

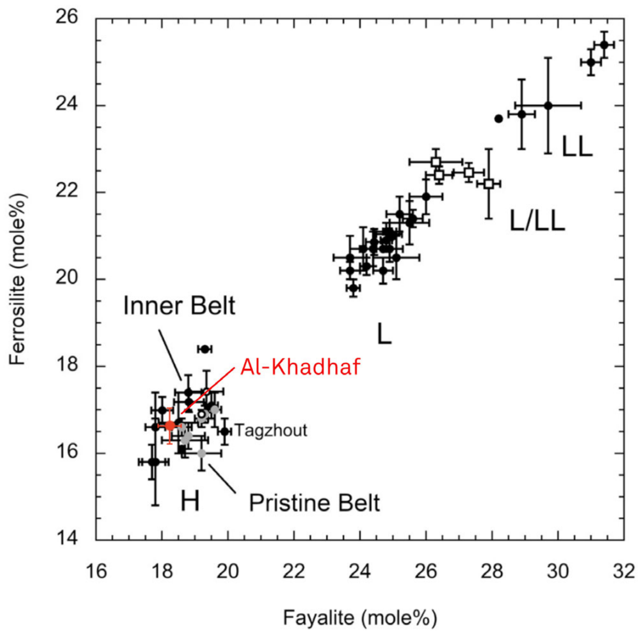

FIGURE 18. The Fa-Fs diagram of ordinary chondrites with the position of Al-Khadhaf marked in red. Modified after Jenniskens and Devillepoix (2025). (Color figure can be viewed at wileyonlinelibrary.com)

CONCLUSIONS

The recovery of a meteorite after 1 year of operation demonstrates the effectiveness of the Oman Meteorite Monitoring Project and confirms that the deserts of Oman are well suited for the recovery of small meteorite falls observed by fireball camera networks. Al-Khadhaf adds an ordinary H chondrite with a well-constrained heliocentric orbit and a cosmogenic exposure age of 8.57 ± 1.2 Ma to the growing data set of instrumentally observed meteorite falls.

Independent trajectory, dark flight, and photometric analyses yield consistent results and enabled the successful recovery of the meteorites. Cosmogenic radionuclide and noble-gas measurements, together with light-curve analysis, constrain the pre-atmospheric size of Al-Khadhaf to the lower end of meteorite-dropping meteoroids, placing it among the smallest camera-observed falls recovered to date.

The combination of CRE age and orbit places Al-Khadhaf within the broad ~7 Ma exposure-age population of H chondrites. While its delivery orbit is consistent with an origin in the inner main belt, current mineralogical, spectral, and dynamical constraints do not uniquely identify a single source family. Both Koronis and inner belt sources such as Massalia remain plausible contributors, highlighting the continued difficulty of linking individual meteorite falls to specific asteroid families.

Each new camera-observed meteorite provides an incremental but important contribution toward understanding the origin, delivery pathways, and flux of meteorites reaching Earth.

Acknowledgments—We are grateful for the support of the Oman Meteorites Monitoring Project by the Ministry of Heritage and Tourism, Muscat. The study was supported by the Swiss National Science Foundation, grant 197247. We thank our colleagues Silas Bosco, Lorenzo Meier, Efraim Elmsholz, and Michele Weber at the Laboratory for High Energy Physics (LHEP)/Albert Einstein Center, University of Bern, for their continuous support to operate the GeMSE facility. Andrey Martynov is thanked for setting up WRF. Pierre Lanari is thanked for giving us access to the micro-CT scanner. Stephan Brechbühl, Nadine Lötscher, and Thomas Aebi are thanked for the thin section preparation. We are grateful for Thomas Schüpbach's focus-stack studio photos of the meteorites. Sophie E. Deam acknowledges the support of an Australian Government Research Training Program Scholarship. The gamma spectrometry analysis was supported by the European Research Council (ERC) grant No. 724320 (ULTIMATE). The micro-CT analysis was supported by the European Research Council (ERC) under the European Union's Horizon 2020 research and innovation program (Grant agreement No. 850530). We also thank M. I. Gritsevich, J. Borovička, and an anonymous reviewer for their constructive and valuable reviews, which helped improve the clarity and quality of this paper. Open access publishing facilitated by Universitat Bern, as part of the Wiley - Universitat Bern agreement via the Consortium Of Swiss Academic Libraries.

Data Availability Statement—Fireball images, astrometric and photometric measurements, trajectory solutions, atmospheric modeling outputs, and 3-D surface models of the recovered meteorites are archived on Zenodo and are publicly available at https://doi.org/10.5281/zenodo.18181404. Electron-microprobe analyses of olivine, pyroxene, feldspar, and chromite are provided as Tables S1–S4 in the online supplementary material.

Editorial handling—Dr. Josep M. Trigo-Rodríguez

REFERENCES

Agostinelli, S., Allison, J., Amako, K., Apostolakis, J., Araujo, H., Arce, P., Asai, M., et al. 2003. Geant4—A Simulation Toolkit. *Nuclear Instruments and Methods in Physics Research Section A: Accelerators, Spectrometers, Detectors and Associated Equipment* 506: 250–303. https://doi.org/10.1016/S0168-9002(03)01368-8.

Alexeev, V. A., Laubenstein, M., Povinec, P. P., and Ustinova, G. K. 2015. Cosmogenic Radionuclides in Chelyabinsk and Kosice Chondrites and Features of Solar Cycles 23 and 24. *Bulletin of the Russian Academy of Sciences: Physics* 79: 596–99. https://doi.org/10.3103/S1062873815050056.

Allison, J., Amako, K., Apostolakis, J., Araujo, H., Arce, D. P., Asai, M., Barrand, G., et al. 2006. Geant4 Developments and Applications. *IEEE Transactions on Nuclear Science* 53: 270–78. https://doi.org/10.1109/TNS.2006.869826.

Allison, J., Amako, K., Apostolakis, J., Arce, P., Asai, M., Aso, T., Bagli, E., et al. 2016. Recent Developments in Geant4. *Nuclear Instruments and Methods in Physics Research Section A: Accelerators, Spectrometers, Detectors and Associated Equipment* 835: 186–225. https://doi.org/10.1016/j.nima.2016.06.125.

Bartoschewitz, R., Appel, P., Barrat, J.-A., Bischoff, A., Caffee, M. W., Franchi, I. A., Gabelica, Z., et al. 2017. The Braunschweig Meteorite – A Recent L6 Chondrite Fall in Germany. *Geochemistry* 77: 207–224. https://doi.org/10.1016/j.chemer.2016.10.004.

Bhandari, N., Bonino, G., Callegari, E., Castagnoli, G. C., Mathew, K. J., Padia, J. T., and Queirazza, G. 1989. The Torino, H6, Meteorite Shower. *Meteoritics* 24: 29–34. https://doi.org/10.1111/j.1945-5100.1989.tb00938.x.

Bischoff, A., Jersek, M., Grau, T., Mirtic, B., Ott, U., Kučera, J., Horstmann, M., et al. 2011. Jesenice—A New Meteorite Fall From Slovenia. *Meteoritics & Planetary Science* 46: 793–804. https://doi.org/10.1111/j.1945-5100.2011.01191.x.

Bizzarri, I., Barghini, D., Colombetti, P., Gardiol, D., Rubinetti, S., Mancuso, S., Di Martino, M., et al. 2023. Cosmogenic Radionuclides in the Cavezzo Meteorite: Gamma-Ray Measurement and Detection Efficiency Simulations. *Applied Radiation and Isotopes* 194: 110651. https://doi.org/10.1016/j.apradiso.2023.110651.

Bland, P. A. 2004. The Desert Fireball Network. *Astronomy and Geophysics* 45: 5.20–5.23. https://doi.org/10.1046/j.1468-4004.2003.45520.x.

Bland, P. A., Smith, T. B., Jull, A. J. T., Berry, F. J., Bevan, A. W. R., Cloudt, S., and Pillinger, C. T. 1996. The Flux of Meteorites to the Earth Over the Last 50 000 Years. *Monthly Notices of the Royal Astronomical Society* 283: 551–565. https://doi.org/10.1093/mnras/283.2.551.

Bland, P. A., Spurný, P., Bevan, A. W. R., Howard, K. T., Towner, M. C., Benedix, G. K., Greenwood, R. C., et al. 2012. The Australian Desert Fireball Network: A New Era for Planetary Science. *Australian Journal of Earth Sciences* 59: 177–187. https://doi.org/10.1080/08120099.2011.595428.

Boaca, I., Gritsevich, M. I., Birlan, M., Nedelcu, A., Boaca, T., Colas, F., Malgoyre, A., Zanda, B., and Vernazza, P. 2022. Characterization of the Fireballs Detected by All-Sky Cameras in Romania. *The Astrophysical Journal* 936: 150. https://doi.org/10.3847/1538-4357/ac8542.

Borovička, J. 1990. The Comparison of Two Methods of Determining Meteor Trajectories From Photographs. *Astronomical Institutes of Czechoslovakia, Bulletin* 41: 391–96.

Borovička, J., Spurný, P., and Shrbený, L. 2020. Two Strengths of Ordinary Chondritic Meteoroids as Derived from Their Atmospheric Fragmentation Modeling. *The Astronomical Journal* 160: 42. https://doi.org/10.3847/1538-3881/ab9608.

Borovička, J., Spurný, P., and Shrbený, L. 2022. Data on 824 Fireballs Observed by the Digital Cameras of the European Fireball Network in 2017–2018: II. Analysis of Orbital and Physical Properties of Centimeter-Sized Meteoroids. *Astronomy & Astrophysics* 667: A158. https://doi.org/10.1051/0004-6361/202244197.

Borovička, J., Spurný, P., Shrbený, L., Štork, R., Kotková, L., Fuchs, J., Keclíková, J., et al. 2022. Data on 824 Fireballs Observed by the Digital Cameras of the European Fireball Network in 2017–2018: I. Description of the Network, Data Reduction Procedures, and the Catalog. *Astronomy & Astrophysics* 667: A157. https://doi.org/10.1051/0004-6361/202244184.

Buhl, S., Toueirjenne, C., Hofmann, B., Laubenstein, M., and Wimmer, K. 2014. The Meteorite Fall Near Boumdeid, Mauritania, from September 14, 2011. *Meteorites* 3: 5–18. https://doi.org/10.5277/MET140101.

Carter, R. T., Jandir, P. S., and Kress, M. E. 2011. Constraining the Drag Coefficients of Meteors in Dark Flight. In: *Proceedings of the Meteoroids 2010 Conference: The Smallest Solar System Bodies held in Breckenridge, Colorado*, pp. 243–250.

Ceplecha, Z. 1975. Ablation and Shape-Density Coefficients in Meteors. *Bulletin of the Astronomical Institutes of Czechoslovakia* 26: 242.

Ceplecha, Z. 1987. Geometric, Dynamic, Orbital and Photometric Data on Meteoroids From Photographic Fireball Networks. *Astronomical Institutes of Czechoslovakia, Bulletin (ISSN 0004-6248)* 38: 222–234.

Ceplecha, Z., Borovička, J., Elford, W. G., ReVelle, D. O., Hawkes, R. L., Porubčan, V., and Šimek, M. 1998. Meteor Phenomena and Bodies. *Space Science Reviews* 84: 327–471. https://doi.org/10.1023/A:1005069928850.

Ceplecha, Z., Spurný, P., Bocek, J., Nováková, M., Polnitzky, K., Porubcan, V., Kirsten, T., and Kiko, J. 1987. European Network Fireballs Photographed in 1978. *Astronomical Institutes of Czechoslovakia, Bulletin (ISSN 0004-6248)* 38: 211–222.

Colas, F., Zanda, B., Bouley, S., Jeanne, S., Malgoyre, A., Birlan, M., Blanpain, C., et al. 2020. FRIPON: A Worldwide Network to Track Incoming Meteoroids. *Astronomy & Astrophysics* 644: A53. https://doi.org/10.1051/0004-6361/202038649.

Cressy, P. J. 1971. Cosmogenic Radionuclides in the Lost City and Ucera Meteorites. *Journal of Geophysical Research* 76: 4072–75. https://doi.org/10.1029/JB076i017p04072.

Dalcher, N., Caffee, M. W., Nishiizumi, K., Welten, K. C., Vogel, N., Wieler, R., and Leya, I. 2013. Calibration of Cosmogenic Noble Gas Production in Ordinary Chondrites Based on ^{36}Cl-^{36}Ar Ages. Part 1: Refined Produced Rates for Cosmogenic ^{21}Ne and ^{38}Ar. *Meteoritics & Planetary Science* 48: 1841–62. https://doi.org/10.1111/maps.12203.

David, J.-C., and Leya, I. 2019. Spallation, Cosmic Rays, Meteorites, and Planetology. *Progress in Particle and Nuclear Physics* 109: 103711. https://doi.org/10.1016/j.ppnp.2019.103711.

Devillepoix, H. A. R., Cupák, M., Sansom, E. K., Towner, M. C., Howie, R. M., Hartig, B. A. D., Jansen-Sturgeon, T., et al. 2020. A Global Fireball Observatory. *Planetary and Space Science* 191: 105036. https://doi.org/10.1016/j.pss.2020.105036.

Dowling, T. E., and Bradley, M. E. 2023. Ram Pressure in Astronomy and Engineering. *Proceedings of the Royal*

Society A: Mathematical, Physical and Engineering Sciences 479: 20220504. https://doi.org/10.1098/rspa.2022.0504.

Drolshagen, E., Ott, T., Koschny, D., Drolshagen, G., Vaubaillon, J., Colas, F., Zanda, B., et al. 2021. Luminous Efficiency Based on FRIPON Meteors and Limitations of Ablation Models. *Astronomy & Astrophysics* 650: A159. https://doi.org/10.1051/0004-6361/202040204.

Eberhardt, P., Eugster, O., Geiss, J., and Marti, K. 1966. Rare Gas Measurements in 30 Stone Meteorites. *Zeitschrift Naturforschung Teil A* 21: 414.

Evans, J. C., Reeves, J. H., Rancitelli, L. A., and Bogard, D. D. 1982. Cosmogenic Nuclides in Recently Fallen Meteorites: Evidence for Galactic Cosmic Ray Variations During the Period 1967–1978. *Journal of Geophysical Research: Solid Earth* 87: 5577–91. https://doi.org/10.1029/jb087ib07p05577.

Gardiol, D., Barghini, D., Buzzoni, A., Carbognani, A., Di Carlo, M., Di Martino, M., Knapic, C., et al. 2020. Cavezzo, the First Italian Meteorite Recovered by the PRISMA Fireball Network. Orbit, Trajectory, and Strewn-Field. *Monthly Notices of the Royal Astronomical Society* 501: 1215–27. https://doi.org/10.1093/mnras/staa3646.

Gattacceca, J., Eisenlohr, P., and Rochette, P. 2004. Calibration of *in situ* Magnetic Susceptibility Measurements. *Geophysical Journal International* 158: 42–49. https://doi.org/10.1111/j.1365-246X.2004.02297.x.

Genge, M. J. 2008. Koronis Asteroid Dust Within Antarctic Ice. *Geology* 36: 687. https://doi.org/10.1130/G24493A.1.

Ghosh, S., Murty, S. V. S., Shukla, P. N., Shukla, A. D., Mahajan, R. R., Bhandari, N., Pant, N. C., Ghosh, J. B., and Shome, S. 2002. Fall, Classification and Cosmogenic Records of the Sabrum (LL6) Chondrite. *Meteoritics & Planetary Science* 37: 439–448. https://doi.org/10.1111/j.1945-5100.2002.tb00826.x.

Graf, T., and Marti, K. 1995. Collisional History of H Chondrites. *Journal of Geophysical Research: Planets* 100: 21247–63. https://doi.org/10.1029/95JE01903.

Gritsevich, M. I. 2008. The Pribram, Lost City, Innisfree, and Neuschwanstein Falls: An Analysis of the Atmospheric Trajectories. *Solar System Research* 42: 372–390. https://doi.org/10.1134/S003809460805002X.

Gritsevich, M. I. 2009. Determination of Parameters of Meteor Bodies Based on Flight Observational Data. *Advances in Space Research* 44: 323–334. https://doi.org/10.1016/j.asr.2009.03.030.

Gritsevich, M. I., Lyytinen, E., Moilanen, J., Kohout, T., Dmitriev, V., Lupovka, V., Midtskogen, V., Kruglikov, N., Ischenko, A., and Yakovlev, G. 2014. First Meteorite Recovery Based on Observations by the Finnish Fireball Network. International Meteor Conference, Giron, France, 18–21 September 2014.

Gritsevich, M. I., Stulov, V. P., and Turchak, L. I. 2012. Consequences of Collisions of Natural Cosmic Bodies With the Earth's Atmosphere and Surface. *Cosmic Research* 50: 56–64. https://doi.org/10.1134/s0010952512010017.

Halliday, I., Blackwell, A. T., and Griffin, A. A. 1978. The Innisfree Meteorite and the Canadian Camera Network. *Journal of the Royal Astronomical Society of Canada* 72: 15–39.

Halliday, I., Griffin, A. A., and Blackwell, A. T. 1996. Detailed Data for 259 Fireballs from the Canadian Camera Network and Inferences Concerning the Influx of Large Meteoroids. *Meteoritics & Planetary Science* 31: 185–217. https://doi.org/10.1111/j.1945-5100.1996.tb02014.x.

Hlobik, F., and Tóth, J. 2024. Orbital Evolution and Possible Parent Asteroids of 40 Instrumentally Observed Meteorites. *Planetary and Space Science* 240: 105827. https://doi.org/10.1016/j.pss.2023.105827.

Hofmann, B. A., and Gnos, E. 2024. The Meteoritic Record of Arabia. *Geological Society, London, Special Publications* 550: SP550-2024-8. https://doi.org/10.1144/sp550-2024-8.

Honda, M., and Arnold, J. R. 1964. Effects of Cosmic Rays on Meteorites: Meteorites are More Suitable than Terrestrial Targets for Studying the Fossil Record of Cosmic Radiation. *Science* 143: 203–212. https://doi.org/10.1126/science.143.3603.203.

Honda, M., Nishiizumi, K., Imamura, M., Takaoka, N., Nitoh, O., Horie, K., and Komura, K. 1982. Cosmogenic Nuclides in the Kirin Chondrite. *Earth and Planetary Science Letters* 57: 101–9. https://doi.org/10.1016/0012-821X(82)90176-5.

Howie, R. M., Paxman, J., Bland, P. A., Towner, M. C., Cupak, M., Sansom, E. K., and Devillepoix, H. A. R. 2017. How to Build a Continental Scale Fireball Camera Network. *Experimental Astronomy* 43: 237–266. https://doi.org/10.1007/s10686-017-9532-7.

Howie, R. M., Paxman, J., Bland, P. A., Towner, M. C., Sansom, E. K., and Devillepoix, H. A. R. 2017. Submillisecond Fireball Timing Using de Bruijn Timecodes. *Meteoritics & Planetary Science* 52: 1669–82. https://doi.org/10.1111/maps.12878.

Jansen-Sturgeon, T., Sansom, E. K., and Bland, P. A. 2019. Comparing Analytical and Numerical Approaches to Meteoroid Orbit Determination Using Hayabusa Telemetry. *Meteoritics & Planetary Science* 54: 2149–62. https://doi.org/10.1111/maps.13376.

Jenniskens, P. 2014. Recent Documented Meteorite Falls, a Review of Meteorite–Asteroid Links. In *Meteoroids 2013: Proceedings of the Astronomical Conference Held at AM University, Poznan*, pp. 57–68.

Jenniskens, P., and Devillepoix, H. A. R. 2025. Review of asteroid, meteor, and meteorite-type links. *Meteoritics & Planetary Science*, 60: 928–973. https://doi.org/10.1111/maps.14321.

Jenniskens, P., Robertson, D., Goodrich, C. A., Shaddad, M. H., Kudoda, A., Fioretti, A. M., and Zolensky, M. E. 2022. Bolide Fragmentation: What Parts of Asteroid 2008 TC_3 Survived to the Ground? *Meteoritics & Planetary Science* 57: 1641–64. https://doi.org/10.1111/maps.13892.

Jenniskens, P., Utas, J., Yin, Q., Matson, R. D., Fries, M., Howell, J. A., Free, D., et al. 2019. The Creston, California, Meteorite Fall and the Origin of L Chondrites. *Meteoritics & Planetary Science* 54: 699–720. https://doi.org/10.1111/maps.13235.

Johnston, C. O., and Stern, E. C. 2024. Assessment of Meteoroid Pre-Atmospheric Diameter From Brightness Measurements Prior to Fragmentation. *Icarus* 408: 115807. https://doi.org/10.1016/j.icarus.2023.115807.

Kimberley, J., and Ramesh, K. T. 2011. The Dynamic Strength of an Ordinary Chondrite. *Meteoritics & Planetary Science* 46: 1653–69. https://doi.org/10.1111/j.1945-5100.2011.01254.x.

Kita, N. T., Welten, K. C., Valley, J. W., Spicuzza, M. J., Nakashima, D., Tenner, T. J., Ushikubo, T., et al. 2013. Fall, Classification, and Exposure History of the Mifflin L5 Chondrite. *Meteoritics & Planetary Science* 48: 641–655. https://doi.org/10.1111/maps.12077.

Kokhirova, G. I., Babadzhanov, P. B., and Khamroev, U. K. 2015. Tajikistan Fireball Network and Results of Photographic Observations. *Solar System Research* 49: 275–283. https://doi.org/10.1134/S0038094615030041.

Komura, K., Inoue, M., and Nakamura, N. 2002. Cosmogenic Radionuclides in the Recently Fallen Kobe (CK4) Meteorite. *Geochemical Journal* 36: 333–340. https://doi.org/10.2343/geochemj.36.333.

Laubenstein, M., Giampaoli, A., Janowski, P., and Mietelski, J. W. 2012. Cosmogenic Radionuclides in the Soøtmany (L6) Meteorite. *Meteorites* 2: 45–51. https://doi.org/10.5277/MET120106.

Leya, I., Ammon, K., Cosarinsky, M., Dalcher, N., Gnos, E., Hofmann, B., and Huber, L. 2013. Light Noble Gases in 12 Meteorites From the Omani Desert, Australia, Mauritania, Canada, and Sweden. *Meteoritics & Planetary Science* 48: 1401–14. https://doi.org/10.1111/maps.12142.

Leya, I., Hirtz, J., and David, J.-C. 2021. Galactic Cosmic Rays, Cosmic-Ray Variations, and Cosmogenic Nuclides in Meteorites. *The Astrophysical Journal* 910: 136. https://doi.org/10.3847/1538-4357/abe52f.

Leya, I., and Masarik, J. 2009. Cosmogenic Nuclides in Stony Meteorites Revisited. *Meteoritics & Planetary Science* 44: 1061–86. https://doi.org/10.1111/j.1945-5100.2009.tb00788.x.

Li, Z., Zou, H., Liu, J., Ma, J., Meng, Q., Cai, Y., Zhao, X., et al. 2024. Multi-station Meteor Monitoring (M^3) System. II. System Upgrade and a Pathfinder Network. *Publications of the Astronomical Society of the Pacific* 136: 114507. https://doi.org/10.1088/1538-3873/ad8597.

Lyytinen, E., and Gritsevich, M. I. 2016. Implications of the Atmospheric Density Profile in the Processing of Fireball Observations. *Planetary and Space Science* 120: 35–42. https://doi.org/10.1016/j.pss.2015.10.012.

Mahajan, R. R. 2022. Noble Gases, Cosmic Ray Exposure and Radiogenic Ages in Selected Ordinary Chondrites. *Advances in Space Research* 70: 2112–32. https://doi.org/10.1016/j.asr.2022.06.037.

Marsset, M., Vernazza, P., Brož, M., Thomas, C. A., DeMeo, F. E., Burt, B., Binzel, R. P., et al. 2024. The Massalia Asteroid Family as the Origin of Ordinary L Chondrites. *Nature* 634: 561–65. https://doi.org/10.1038/s41586-024-08007-6.

McFadden, L., Brown, P. G., and Vida, D. 2024. A Comparison of Fireball Luminous Efficiency Models Using Acoustic Records. *Icarus* 422: 116250. https://doi.org/10.1016/j.icarus.2024.116250.

McMullan, S., Vida, D., Devillepoix, H. A. R., Rowe, J., Daly, L., King, A. J., Cupák, M., et al. 2024. The Winchcombe Fireball—That Lucky Survivor. *Meteoritics & Planetary Science* 59: 927–947. https://doi.org/10.1111/maps.13977.

Mészáros, M., Leya, I., Hofmann, B. A., and Szidat, S. 2018. Current Performance and Preliminary Results of a New ^{14}C Extraction Line for Meteorites at the University of Bern. *Radiocarbon* 60: 601–615. https://doi.org/10.1017/rdc.2017.114.

National Centers For Environmental Prediction (National Weather Service/NOAA/U.S. Department of Commerce). 2000. NCEP FNL Operational Model Global Tropospheric Analyses, Continuing From July 1999 https://doi.org/10.5065/D6M043C6.

Nesvorný, D., Deienno, R., Bottke, W. F., Jedicke, R., Naidu, S., Chesley, S. R., Chodas, P. W., et al. 2023. NEOMOD: A New Orbital Distribution Model for Near-Earth Objects. *The Astronomical Journal* 166: 55. https://doi.org/10.3847/1538-3881/ace040.

Nishiizumi, K., Regnier, S., and Marti, K. 1980. Cosmic Ray Exposure Ages of Chondrites, Pre-Irradiation and Constancy of Cosmic Ray Flux in the Past. *Earth and Planetary Science Letters* 50: 156–170. https://doi.org/10.1016/0012-821X(80)90126-0.

Oberst, J., Molau, S., Heinlein, D., Gritzner, C., Schindler, M., Spurny, P., Ceplecha, Z., Rendtel, J., and Betlem, H. 1998. The "European Fireball Network": Current Status and Future Prospects. *Meteoritics & Planetary Science* 33: 49–56. https://doi.org/10.1111/j.1945-5100.1998.tb01606.x.

Picone, J. M., Hedin, A. E., Drob, D. P., and Aikin, A. C. 2002. NRLMSISE-00 Empirical Model of the Atmosphere: Statistical Comparisons and Scientific Issues. *Journal of Geophysical Research: Space Physics* 107: SIA15-1–SIA15-16. https://doi.org/10.1029/2002JA009430.

Pohl, L., and Britt, D. T. 2020. Strengths of Meteorites—An Overview and Analysis of Available Data. *Meteoritics & Planetary Science* 55: 962–987. https://doi.org/10.1111/maps.13449.

Popova, O., Borovička, J., Hartmann, W. K., Spurný, P., Gnos, E., Nemtchinov, I., and Trigo-Rodríguez, J. M. 2011. Very Low Strengths of Interplanetary Meteoroids and Small Asteroids. *Meteoritics & Planetary Science* 46: 1525–50. https://doi.org/10.1111/j.1945-5100.2011.01247.x.

Povinec, P. P., Masarik, J., Sýkora, I., Kováčik, A., Beňo, J., Meier, M. M. M., Wieler, R., Laubenstein, M., and Porubčan, V. 2015. Cosmogenic Nuclides in the Košice Meteorite: Experimental Investigations and Monte Carlo Simulations. *Meteoritics & Planetary Science* 50: 880–892. https://doi.org/10.1111/maps.12380.

Ramírez, G. D., Baur, D., Grigat, J., Hofmann, B. A., Lindemann, S., Masson, D., Schumann, M., Von Sivers, M., and Toschi, F. 2022. GeMSE: a low-Background Facility for Gamma-Spectrometry at Moderate Rock Overburden. *Journal of Instrumentation* 17: P04005. https://doi.org/10.1088/1748-0221/17/04/p04005.

Ray, D., Mahajan, R. R., Shukla, A. D., Goswami, T. K., and Chakraborty, S. 2017. Petrography, Classification, Oxygen Isotopes, Noble Gases, and Cosmogenic Records of Kamargaon (L6) Meteorite: The Latest Fall in India. *Meteoritics & Planetary Science* 52: 1744–53. https://doi.org/10.1111/maps.12875.

Revelle, D. O., and Ceplecha, Z. 2001. Bolide Physical Theory With Application to PN and EN Fireballs. In *Meteoroids 2001 Conference*, ESA Special Publication, Los Alamos National Laboratory, New Mexico, 507–512.

Rosén, Å. V., Hofmann, B. A., Preusser, F., Gnos, E., Eggenberger, U., Schumann, M., and Szidat, S. 2021. Meteorite Terrestrial Ages in Oman Based on Gamma Spectrometry and Sediment Dating, Focusing on the Ramlat Fasad Dense Collection Area. *Meteoritics & Planetary Science* 56: 2017–34. https://doi.org/10.1111/maps.13758.

Rosén, Å. V., Hofmann, B. A., Von Sivers, M., and Schumann, M. 2020. Radionuclide Activities in Recent Chondrite Falls Determined by Gamma-Ray Spectrometry: Implications for Terrestrial Age Estimates. *Meteoritics & Planetary Science* 55: 149–163. https://doi.org/10.1111/maps.13427.

Sanchez, J. A., Reddy, V., Dykhuis, M., Lindsay, S., and Corre, L. L. 2015. Composition of Potentially Hazardous Asteroid (214869) 2007 PA8: An H Chondrite From the Outer Asteroid Belt. *The Astrophysical Journal* 808: 93. https://doi.org/10.1088/0004-637X/808/1/93.

Sansom, E. K., Bland, P., Paxman, J., and Towner, M. 2015. A Novel Approach to Fireball Modeling: The Observable and the Calculated. *Meteoritics & Planetary Science* 50: 1423–35. https://doi.org/10.1111/maps.12478.

Sansom, E. K., Bland, P. A., Towner, M. C., Devillepoix, H. A. R., CupÁk, M., Howie, R. M., Jansen-Sturgeon, T., et al. 2020. Murrili Meteorite's Fall and Recovery From Kati Thanda. *Meteoritics & Planetary Science* 55: 2157–68. https://doi.org/10.1111/maps.13566.

Sansom, E. K., Gritsevich, M. I., Devillepoix, H. A. R., Jansen-Sturgeon, T., Shober, P., Bland, P. A., Towner, M. C., Cupák, M., Howie, R. M., and Hartig, B. A. D. 2019. Determining Fireball Fates Using the α–β Criterion. *The Astrophysical Journal* 885: 115. https://doi.org/10.3847/1538-4357/ab4516.

Sansom, E. K., Jansen-Sturgeon, T., Rutten, M. G., Devillepoix, H. A. R., Bland, P. A., Howie, R. M., Cox, M. A., Towner, M. C., Cupák, M., and Hartig, B. A. D. 2019. 3D Meteoroid Trajectories. *Icarus* 321: 388–406. https://doi.org/10.1016/j.icarus.2018.09.026.

Shober, P. M., Devillepoix, H. A. R., Sansom, E. K., Towner, M. C., Cupák, M., Anderson, S. L., Benedix, G., et al. 2022. Arpu Kuilpu: An H5 From the Outer Main Belt. *Meteoritics & Planetary Science* 57: 1146–57. https://doi.org/10.1111/maps.13813.

Shober, P. M., Vaubaillon, J., Devillepoix, H. A. R., Sansom, E. K., Deam, S. E., Anghel, S., Colas, F., Vernazza, P., and Zanda, B. 2025. What Falls Versus What We Recover: Quantifying Search and Recovery Bias for Orbital Meteorites. *Meteoritics & Planetary Science* 60: 2488–2503. https://doi.org/10.1111/maps.70041.

Sivers, M. V., Hofmann, B. A., Rosén, Å. V., and Schumann, M. 2016. The GeMSE Facility for Low-Background γ-Ray Spectrometry. *Journal of Instrumentation* 11: P12017. https://doi.org/10.1088/1748-0221/11/12/P12017.

Skamarock, W., Klemp, J., Dudhia, J., Gill, D., Barker, D., Wang, W., Huang, X.-Y., and Duda, M. 2008. *A Description of the Advanced Research WRF Version 3*. National Center for Atmospheric Research, Boulder. https://doi.org/10.5065/D68S4MVH.

Skamarock, W. C., Klemp, J. B., Dudhia, J., Gill, D. O., Liu, Z., Berner, J., Wang, W., et al. 2019. *A Description of the Advanced Research WRF Model Version 4*. National Center for Atmospheric Research, Boulder. https://doi.org/10.5065/1DFH-6P97.

Spurný, P., Borovička, J., and Shrbený, L. 2006. Automation of the Czech Part of the European Fireball Network: Equipment, Methods and First Results. *Proceedings of the International Astronomical Union* 2: 121–130. https://doi.org/10.1017/S1743921307003146.

Subasinghe, D., Campbell-Brown, M., and Stokan, E. 2017. Luminous Efficiency Estimates of Meteors–I. Uncertainty analysis. *Planetary and Space Science* 143: 71–77. https://doi.org/10.1016/j.pss.2016.12.009.

Tauseef, M., Leya, I., Gattacceca, J., Hofmann, B., Szidat, S., Braucher, R., and ASTER Team. 2024. ^{14}C and ^{14}C-^{10}Be Terrestrial Age Dating System for Meteorites—New Data for Four Recently Fallen Meteorites. *Meteoritics & Planetary Science* 59: 1219–35. https://doi.org/10.1111/maps.14144.

Tauseef, M., Leya, I., Gattacceca, J., Szidat, S., Braucher, R., Kruttasch, P. M., Zappatini, A., and ASTER Team. 2025. Evaluating ^{14}C and ^{14}C-^{10}Be Terrestrial Age Dating Systems for Meteorites Using Experimental Data and Model Calculations. *Meteoritics & Planetary Science* 60: 1263–83. https://doi.org/10.1111/maps.14355.

Towner, M. C., Cupak, M., Deshayes, J., Howie, R. M., Hartig, B. A. D., Paxman, J., Sansom, E. K., Devillepoix, H. A. R., Jansen-Sturgeon, T., and Bland, P. A. 2020. Fireball Streak Detection With Minimal CPU Processing Requirements for the Desert Fireball Network Data Processing Pipeline. *Publications of the Astronomical Society of Australia* 37: e008. https://doi.org/10.1017/pasa.2019.48.

Towner, M. C., Jansen-Sturgeon, T., Cupak, M., Sansom, E. K., Devillepoix, H. A. R., Bland, P. A., Howie, R. M., Paxman, J. P., Benedix, G. K., and Hartig, B. A. D. 2022. Dark-Flight Estimates of Meteorite Fall Positions: Issues and a Case Study Using the Murrili Meteorite Fall. *The Planetary Science Journal* 3: 44. https://doi.org/10.3847/psj/ac3df5.

Trigo-Rodríguez, J. M., Llorca, J., Castro-Tirado, A. J., Ortiz, J. L., Docobo, J. A., and Fabregat, J. 2006. The Spanish Fireball Network. *Astronomy & Geophysics* 47: 6.26–6.28. https://doi.org/10.1111/j.1468-4004.2006.47626.x.

Turchak, L. I., and Gritsevich, M. I. 2014. Meteoroids Interaction With The Earth Atmosphere. *Journal of Theoretical and Applied Mechanics* 44: 15–28. https://doi.org/10.2478/jtam-2014-0020.

Tymiński, Z., Hult, M., Krzesińska, A. M., Tymińska, K., Lutter, G., Saganowski, P., Marissens, G., et al. 2023. Underground Radioactivity Measurements of Meteorites: Development of Methods Suitable to Determine Precise Terrestrial Age of Recent Falls. *Applied Radiation and Isotopes* 195: 110733. https://doi.org/10.1016/j.apradiso.2023.110733.

Vida, D., Šegon, D., Gural, P. S., Brown, P. G., McIntyre, M. J. M., Dijkema, T. J., Pavletić, L., et al. 2021. The Global Meteor Network – Methodology and First Results. *Monthly Notices of the Royal Astronomical Society* 506: 5046–74. https://doi.org/10.1093/mnras/stab2008.

Wasson, J. T., and Kallemeyn, G. W. 1988. Compositions of Chondrites. *Philosophical Transactions of the Royal Society of London. Series A, Mathematical and Physical Sciences* 325: 535–544. https://doi.org/10.1098/rsta.1988.0066.

Weryk, R. J., Brown, P. G., Domokos, A., Edwards, W. N., Krzeminski, Z., Nudds, S. H., and Welch, D. L. 2008. The Southern Ontario All-Sky Meteor Camera Network. In *Advances in Meteoroid and Meteor Science*, edited by J. M. Trigo-Rodríguez, F. J. M. Rietmeijer, J. Llorca, and D. Janches, 241–46. New York, NY: Springer New York.

Wetherill, G. W., and ReVelle, D. O. 1981. Which Fireballs are Meteorites? A Study of the Prairie Network Photographic Meteor Data. *Icarus* 48: 308–328. https://doi.org/10.1016/0019-1035(81)90112-3.

Wieler, R. 2002. Noble Gases in the Solar System. *Reviews in Mineralogy and Geochemistry* 47: 21–70. https://doi.org/10.2138/rmg.2002.47.2.

Wiśniewski, M., Żoøądek, P., Olech, A., Tyminski, Z., Maciejewski, M., Fietkiewicz, K., Rudawska, R., et al. 2017. Current Status of Polish Fireball Network. *Planetary and Space Science* 143: 12–20. https://doi.org/10.1016/j.pss.2017.03.013.

Wrigley, R. C. 1971. Some Cosmogenic Radionuclides in the Lost City Meteorite. *Journal of Geophysical Research* 76: 4124–26. https://doi.org/10.1029/JB076i017p04124.

SUPPORTING INFORMATION

Additional supporting information may be found in the online version of this article.

Data S1. Electron microprobe analyses of olivine, pyroxene, feldspar and chromite.